

Mass Profile of the Infall Region of the Abell 2199 Supercluster

K. Rines¹, M.J. Geller², A. Diaferio³, A. Mahdavi^{4,5}, J.J. Mohr⁶, and G. Wegner⁷

krines@cfa.harvard.edu

ABSTRACT

Using a redshift survey of 1323 galaxies (1092 new or remeasured) in a region of 95 square degrees centered on the nearby galaxy cluster Abell 2199, we analyze the supercluster containing A2199, A2197, and an X-ray group. The caustic technique accurately reproduces the true mass profiles of simulated simple superclusters (i.e., superclusters where the virial mass of one cluster is 2-10 times the virial mass of all other clusters in the supercluster). We calculate the masses of the two main components of A2197 (A2197W and A2197E) using archival X-ray observations and demonstrate that the A2199 supercluster is simple (the mass of A2199 is 5 and 12 times larger than A2197W and A2197E respectively) and thus that the caustic technique should yield an accurate mass profile. The masses of A2199, A2197W, and A2197E within r_{500} (the radius within which the enclosed density is 500 times the critical density) are 22.0, 3.8, and $1.7 \times 10^{13} h^{-1} M_{\odot}$. The mass profile is uncertain by $\sim 30\%$ within $3 h^{-1} \text{Mpc}$ and by a factor of two within $8 h^{-1} \text{Mpc}$ and is one of only a few for a supercluster on such large scales. Independent X-ray mass estimates agree with our results at all radii where they overlap. The mass profile strongly disagrees with an isothermal sphere profile but agrees with profiles suggested by simulations. We discuss the interplay of

¹Harvard-Smithsonian Center for Astrophysics, 60 Garden St, Cambridge, MA 02138 ; krines@cfa.harvard.edu

²Smithsonian Astrophysical Observatory; mgeller@cfa.harvard.edu

³Università degli Studi di Torino, Dipartimento di Fisica Generale "Amedeo Avogadro", Torino, Italy; diaferio@ph.unito.it

⁴Institute for Astronomy, University of Hawaii, 2680 Woodlawn Drive, Honolulu, HI 96822

⁵Chandra Fellow

⁶Departments of Astronomy and Physics, University of Illinois, 1002 W. Green St. Urbana, IL 61801; jmohr@uiuc.edu

⁷Department of Physics and Astronomy, Dartmouth College, Hanover, NH 03755; gaw@bellz.dartmouth.edu

the supercluster dynamics and the dynamics of the bound subclusters. The agreement between the infall mass profile and other techniques shows that the caustic technique is surprisingly robust for simple superclusters.

Subject headings: galaxies: clusters: individual (A2199, A2197) — galaxies: kinematics and dynamics — cosmology: observations

1. Introduction

Clusters of galaxies are important probes of the distribution of matter on intermediate scales. Clusters are surrounded by infall regions where the galaxies are falling into the gravitational potential well of the cluster, but have not yet reached equilibrium. Many, perhaps most, of the galaxies in this region are on their first pass through the cluster. They populate a regime between that of relaxed cluster cores and the surrounding large-scale structure where the transition from linear to non-linear clustering occurs. Recent papers have explored infall regions using two-body dynamics of binary clusters (e.g., Mohr & Wegner 1997), the virial theorem in superclusters (Small et al. 1998), and weak lensing (Kaiser et al. 2002). Ellingson et al. (2001) demonstrate that these infall regions are the site of significant galaxy evolution and are key to understanding the Butcher-Oemler (Butcher & Oemler 1984) effect. Two recent papers (Reisenegger et al. 2000; Rines et al. 2001b) demonstrate that the infall regions of clusters (the Shapley Supercluster and Abell 2199 respectively) provide evidence of hierarchical structure formation on supercluster scales.

Because clusters are not in equilibrium outside the virial radius, neither X-ray observations nor virial analysis provide accurate mass determinations at large radii. There are now two methods of approaching this problem: weak gravitational lensing (Kaiser et al. 2002) and kinematics of the infall region (Diaferio & Geller 1997; Diaferio 1999, hereafter DG and D99 respectively). In redshift space, the infall regions of clusters form a characteristic trumpet-shaped pattern. These caustics arise because galaxies fall into the cluster as the cluster potential overwhelms the Hubble flow (Kaiser 1987; Regös & Geller 1989). Under simple spherical infall, the galaxy phase space density becomes infinite at the caustics. DG analyzed the dynamics of infall regions with numerical simulations and found that in the outskirts of clusters, random motions due to substructure and non-radial motions make a substantial contribution to the amplitude of the caustics which delineate the infall regions (see also Vedel & Hartwick 1998). DG showed that the amplitude of the caustics is a measure of the escape velocity from the cluster; identification of the caustics therefore allows a determination of the mass profile of the cluster beyond the virial radius. DG find that nonparametric measurements of caustics in simulated clusters yield mass profiles accurate

to $\sim 50\%$ on scales up to $10 h^{-1}\text{Mpc}$.

The caustic technique places no requirements on the equilibrium state of the cluster; rather, it assumes only that galaxies trace the velocity field. Indeed, simulations suggest that little or no velocity bias exists on linear and mildly non-linear scales (Kauffmann et al. 1999a,b). Vedel & Hartwick (1998) used simulations to explore an alternative parametric analysis of the infall region using a maximum likelihood method. Their technique requires assumptions about the functional forms of the density profile and the velocity dispersion profile. Geller et al. (1999, hereafter GDK) applied the kinematic method of DG to the infall region of the Coma cluster. They successfully reproduced the X-ray derived mass profile and extended direct determinations of the mass profile to $\sim 10 h^{-1}\text{Mpc}$. This method has also been applied to the Shapley Supercluster (Reisenegger et al. 2000), A576 (Rines et al. 2000), A1644 (Tustin et al. 2001) and the Fornax cluster (Drinkwater et al. 2001).

We apply the method of DG and D99 to A2199, one of the richest, most regular nearby clusters of galaxies (Markevitch et al. 1999, hereafter MVFS). Rines et al. (2001b) presented a preliminary view of this system and demonstrated that it contains several infalling, bound subclusters. This system provides an important test of the robustness of the caustic technique in simple superclusters (i.e., those dominated by a cluster 2-10 times more massive than any other system in the supercluster).

We describe numerical simulations of simple superclusters in § 2 to demonstrate the validity of the caustic technique for these systems. We describe the spectroscopic observations in § 3. In § 4, we show that A2197 is a superposition of groups and demonstrate that A2199/A2197 is indeed a simple supercluster. We determine the amplitude of the caustics, calculate the mass profile, and compare the infall mass profile to other estimators in § 5. We discuss our results in § 6 and conclude in § 7. The physical scale at the redshift of the supercluster ($cz = 9156 \text{ km s}^{-1}$) is $1^\circ = 1.54 h^{-1}\text{Mpc}$ ($H_0 = 100 h \text{ km s}^{-1}$, $\Omega_m = 0.3$, $\Omega_\Lambda = 0.7$).

2. Simulations of Simple Superclusters

The caustic technique as developed by D99 is successful in reproducing the mass profiles of isolated clusters. Before applying the technique to more complex systems, we need to verify that this technique still produces accurate mass profiles in the presence of significant substructure in the infall region. We extracted three simple superclusters from the ΛCDM cosmological simulation of the GIF collaboration, where galaxy formation and evolution within dark matter halos are modelled with a semi-analytic technique (Kauffmann et al. 1999a,b). Here, we define simple superclusters as those dominated by a cluster 2-10 times

more massive than any other systems in the supercluster. These three systems have mass, M_1 , within r_{200} (roughly equivalent to the virial mass) for the central system greater than $10^{14}h^{-1}M_\odot$; the next largest subhalo has a mass M_2 between $10^{13}h^{-1}M_\odot$ and $10^{14}h^{-1}M_\odot$ and lies outside the virial radius of the main cluster. Table 1 lists the properties of the simulated superclusters. Column [1] gives the system ID, Column [2] is the mass M_1 of the largest system in the supercluster, Column [3] is the mass ratio M_1/M_2 , Column [4] and Column [5] list the mass and 3-D distance of the four subhalos (with $M > 10^{13}h^{-1}M_\odot$) closest to the largest system. The mass ratio M_1/M_2 ranges between 2 and 6 to investigate the sensitivity of the mass estimator to companions of various relative sizes. We restrict our analysis to Λ CDM simulations because these more accurately reproduce the appearance of the observed caustics in nearby systems (see references in §1); caustics in τ CDM simulations are less well-defined. D99 suggests that the degree of delineation of the caustics is a cosmological indicator; caustics are better defined (have fewer interlopers) in low- Ω_m universes because the accretion rate in the present epoch decreases with decreasing Ω_m .

Figures 1-3 display the caustics (calculated according to the prescription of D99) for these systems as viewed from three different lines of sight. Redshift diagrams include all galaxies brighter than $M_B = -18.5 + 5\log h$. As in isolated clusters (D99), some lines of sight are more favorable than others. Figure 4 compares the mass profiles inferred from the caustics to the true radial mass profiles. Figure 5 shows the difference between the estimated and true mass profiles in units of the uncertainty in the estimated mass. The estimated mass differs by more than $2\text{-}\sigma$ only for some lines of sight to the supercluster with $M_1/M_2 = 2.0$. The bias in the mass estimates appears to be small, although the small number of systems considered prevents firm conclusions. Thus, the caustic method is robust to the presence of massive subhalos provided the mass ratio (measured within r_{200}) is greater than about 2.0. We show in §4 that A2197 (actually A2197W+A2197E) is much less massive than A2199, the caustic technique should thus yield an accurate mass profile for the A2199 supercluster.

2.1. Model Mass Profiles

We now investigate whether the mass profiles of the simulated simple superclusters are well described by simple analytic models. The simplest model of a self-gravitating system is a singular isothermal sphere (SIS). The mass of the SIS increases linearly with radius. Navarro et al. (1997) and Hernquist (1990) propose two-parameter models based on CDM simulations of haloes. At large radii, the NFW mass profile increases as $\ln(r)$ and the mass

of the Hernquist model converges. The NFW mass profile is

$$M(< r) = \frac{M(a)}{\ln(2) - \frac{1}{2}} \left[\ln\left(1 + \frac{r}{a}\right) - \frac{r}{a+r} \right] \quad (1)$$

where a is the scale radius and $M(a)$ is the mass within a . We fit the parameter $M(a)$ rather than the characteristic density δ_c ($M(a) = 4\pi\delta_c\rho_c a^3[\ln(2) - \frac{1}{2}]$ where ρ_c is the critical density) because $M(a)$ and a are much less correlated than δ_c and a . The Hernquist mass profile is

$$M(< r) = M \frac{r^2}{(r+a)^2} \quad (2)$$

where a is the scale radius and M is the total mass. Note that $M(a) = M/4$. The SIS mass profile is

$$M(< r) = M(a = 0.5 h^{-1}\text{Mpc}) \frac{r}{0.5 h^{-1}\text{Mpc}} \quad (3)$$

where we arbitrarily set the scale radius $a = 0.5 h^{-1}\text{Mpc}$. We assume 10% uncertainties in the true mass profiles and minimize χ^2 . Table 2 lists the best-fit parameters a (fixed for SIS) and $M(a)$ for the three models for the simulated superclusters. Because the individual points in the mass profile are not independent, the absolute values of χ^2_ν listed in Table 2 are indicative only, but it is clear that the NFW and Hernquist profiles provide acceptable fits to the infall mass profile; the SIS is excluded for all estimates. The NFW profile generally provides a better fit to the data than the Hernquist profile. A non-singular isothermal sphere mass profile yields results similar to the SIS; thus, we only report our results for the SIS.

3. Observations

3.1. Spectroscopy

We have collected 1323 redshifts (1092 new or remeasured) in a large region (95 square degrees) surrounding A2199/A2197. Two of us (JJM and GW) used the Decaspec (Fabricant & Hertz 1990) at the 2.4-m MDM telescope on Kitt Peak to obtain 246 redshifts of galaxies in the central $1^\circ \times 1^\circ$ of this region for a separate Jeans analysis of the central region of A2199 (Mohr et al. in preparation).

We used the FAST spectrograph (Fabricant et al. 1998) on the 1.5-m Tillinghast telescope of the Fred Lawrence Whipple Observatory (FLWO) to measure 820 spectra of galaxies within $5^\circ.5$ ($\approx 8.5 h^{-1}\text{Mpc}$) of the center of A2199. FAST is a high throughput, long slit spectrograph with a thinned, backside illuminated, antireflection coated CCD detector. The slit length is $180''$; our observations used a slit width of $3''$ and a $300 \text{ lines mm}^{-1}$ grating.

This setup yields spectral resolution of 6-8 Å and covers the wavelength range 3600-7200 Å. We obtain redshifts by cross-correlation with spectral templates of emission-dominated and absorption-dominated galaxy spectra created from FAST observations (Kurtz & Mink 1998).

We observed infall galaxy candidates in three campaigns. We selected targets from digitized images of the POSS I. We initially selected galaxies using the automatic classification system of the Automated Plate Scanner (APS)⁸; we visually inspected these targets to eliminate stars. The first campaign yielded a deep sample in the central $4^\circ \times 4^\circ$ region around A2199. This sample is complete to 103aE magnitude $E < 16.5$ and consists of 304 redshifts. The second campaign (379 redshifts) is a shallower survey ($E < 16.1$) of all galaxies within $5.5 \approx 8.5 h^{-1}\text{Mpc}$ of A2199. The third campaign added 137 redshifts for galaxies which were excluded from the APS catalog for unknown reasons (§3.2). The completeness limits are imprecise because the magnitudes come from multiple plate scans and because we could not obtain redshifts for some low surface brightness galaxies. We include 84 redshifts associated with the groups NRGs385 and NRGs388 obtained with FAST for a separate study of the X-ray and optical properties of groups of galaxies (59 published in Mahdavi et al. 1999, 2000, hereafter MBGR).

We collected the remaining redshifts from the Updated Zwicky Catalogue (Falco et al. 1999, 158 redshifts) with a small number (15) from other sources listed in the NASA/IPAC Extragalactic Database⁹ (Kirshner et al. 1983; Strauss & Huchra 1988; de Vaucouleurs et al. 1991; Freudling et al. 1992; Zabludoff et al. 1993; Haynes et al. 1997; Hill & Oegerle 1998). Table 3 contains our redshift data. The table includes all redshifts obtained with FAST and from the literature as well as redshifts obtained with Decaspec for all galaxies brighter than $E=16.1$ (the remaining 188 will appear in Mohr et al. in preparation). This catalog is complete to $E=16.1$ within 5.5 of the center of A2199 and includes 38 galaxies outside 5.5 but within $6.5 \approx 10 h^{-1}\text{Mpc}$ (Figure 6, described in detail in §5).

3.2. APS Catalog – Photometry and Incompleteness

When matching galaxies from our redshift catalog with a galaxy catalog from APS, we discovered that several nearby, bright galaxies including NGC 6160 (a cD galaxy in A2197) are not classified as galaxies by the APS neural network. A further search reveals that the

⁸The APS databases are supported by the National Aeronautics and Space Administration and the University of Minnesota, and are available at <http://aps.umn.edu>

⁹The NASA/IPAC Extragalactic Database is available at <http://nedwww.ipac.caltech.edu/index.html>

APS identified many of these objects but incorrectly classified them as stars. The default magnitude listed for these objects is from the magnitude-diameter relationship for stars (Humphreys et al. 1991). Because galaxies have large diameters, they are assigned bright magnitudes. We extracted a catalog of all objects classified as stars by APS with magnitudes $E_{diam} < 12$ within $5.^\circ 5$ of A2199. Visual inspection of these 4876 objects yielded 160 galaxies (5 of which are star-galaxy blends), suggesting a misclassification rate of $\sim 3.3\%$. Because these objects include bright, large galaxies like NGC 6160, the incompleteness in the APS could be significant in nearby galaxy surveys.

Because of these difficulties, we reanalyzed the POSS I 103aE (red) plates using SExtractor to calculate object parameters and magnitudes. We calculated the mean offset between SExtractor MAGBEST magnitudes and the isophotal magnitudes in the APS catalog to determine the zero point for each plate. We next identified galaxy candidates as objects with MAGBEST < 16.5 , staricity parameter smaller than 0.5, and ISO7/ISO2 greater than 0.35. ISO1-7 are the numbers of pixels included within various isophotes; the latter criterion thus selects extended objects. We ran SExtractor in CCD mode. We experimented with running SExtractor in PHOTO mode (appropriate for photographic plates) after taking the logarithm of the scanned image (this step is needed to obtain a sufficiently small dynamic range for this mode) and found nearly identical results for both photometric and shape parameters.

Finally, we visually inspected all galaxy candidates to compile a complete catalog of galaxies brighter than $E = 16.1$. Our new catalog includes 970 galaxies, 135 (14%) of which are not included in the APS catalog. These 970 galaxies comprise the majority (71%) of the redshift sample; the fainter galaxies in the remainder of the sample are located mainly near A2199, A2197, and the X-ray groups NRGs385 and NRGs388.

3.3. X-Ray Data

Archival X-ray observations are available for the entire A2199 supercluster from the *ROSAT* All-Sky Survey (Voges et al. 1999). Several longer pointed observations of selected parts of the supercluster are available in the *ROSAT* PSPC and *ASCA* archives (Table 4). Feretti et al. (1995) discuss radio and *ROSAT* pointed observations of the groups NRGs385 and NRGs388. We calculate the luminosities of the systems in the *ROSAT* energy band (Table 5) from the pointed observations assuming that all of the subsystems are at the distance of A2199 ($cz = 9156 \text{ km s}^{-1}$, see §5). We used the X-ray analysis package ZHTOOLS¹⁰ to extract regions around the sources, subtract background sources, and correct for vignetting

¹⁰Available at <http://hea-www.harvard.edu/alexey/zhtools/>

and the exposure maps. We then used PIMMS¹¹ to convert PSPC count rates into fluxes. We assumed Galactic column density and a Raymond-Smith thermal plasma with an abundance of 0.4 and $kT = 4.5$ keV for A2199 (MVFS), 0.2/1.7 keV for A2197W, and 0.2/1.0 keV for all others (see §5.2). Figure 6 displays the RASS data in a large area around A2199 after correcting for the exposure map and smoothing with a Gaussian with a FWHM of $2'$.

4. A2197: An Optically Rich “Cluster” Composed of Superposed Groups

A2197 has been observed by both *ROSAT* and *ASCA*. Figure 7 shows X-ray contours of the 13.5-ksec combined archival *ROSAT* PSPC observation of A2197 (Table 4) overlaid on an optical image from POSS I. The X-ray contours clearly show the presence of West-East components separated by $24'$ centered on NGC 6160 and NGC 6173 respectively (Muriel et al. 1996). The galaxy contours (Figure 6) show at least two distinct NW-SE components, but the galaxy distribution is skewed with respect to the X-ray emission (see also Rines et al. 2001b). Because the intragroup gas is expected to better trace the gravitational potential, we use the X-ray centers in all subsequent analysis.

We find several distinct X-ray sources in the combined PSPC observation of A2197. Table 6 lists the X-ray luminosities of sources with obvious optical counterparts. In addition to A2197W and A2197E, we identify five galaxies in or near A2197, one background galaxy, two background Abell clusters (A2187 and A2196), and two background QSOs. A2187 is recognized as an X-ray cluster (Ebeling et al. 2000; Böhringer et al. 2000) but our determination of the X-ray luminosity of A2196 is new. The galaxies have X-ray luminosities of $L_X(0.1 - 2.4 \text{ keV}) = 4 - 64 \times 10^{40} h^{-2} \text{ erg s}^{-1}$, within the range of isolated bright galaxies (Mahdavi & Geller 2001).

4.1. Redshift Distribution

A2197 shows significant substructure in redshift space. Figure 8 shows a redshift histogram of galaxies within $1.5 h^{-1} \text{ Mpc}$ of A2197W with a bin size of 200 km s^{-1} . We calculate $\chi^2 = 36.3$ for 12 degrees of freedom, indicating that the parent redshift distribution is non-Gaussian at the 99.9% confidence level. A two-component Gaussian fit yields $\chi^2 = 10.8$ for 9 degrees of freedom, an acceptable fit. The properties of the best-fit components are $N_1 = 82 \pm 5$, $\mu_1 = 8787 \pm 33 \text{ km s}^{-1}$, $\sigma_1 = 361 \pm 26 \text{ km s}^{-1}$, and $N_2 = 48 \pm 6$,

¹¹Available at <http://heasarc.gsfc.nasa.gov/docs/software/tools/pimms.html>

$$\mu_2 = 9800 \pm 35 \text{ km s}^{-1}, \sigma_2 = 365 \pm 78 \text{ km s}^{-1},$$

We recalculate the mean redshifts and velocity dispersions of the two subclusters according to the prescription of Danese et al. (1980) but with a limiting radius of $0.25 h^{-1}\text{Mpc}$, which is small enough that the groups do not overlap. The mean redshifts of A2197W and A2197E are $9569 \pm 151 \text{ km s}^{-1}$ and $8919 \pm 153 \text{ km s}^{-1}$ based on 11 and 10 members respectively. The mean redshifts differ by $4.2\text{-}\sigma$. A K-S test indicates that the redshifts are drawn from different populations at the 99.6% confidence level. Note that the redshifts of NGC 6160 and NGC 6173 are 9408 km s^{-1} and 8842 km s^{-1} respectively (Table 3), suggesting that they may lie near the centers of the two groups (Figure 8).

These tests show that the groups A2197W and A2197E are separated in redshift space. The two groups overlap each other both on the sky and in redshift space; they may be interacting in the current epoch. Apparently, A2197E is a richer group than A2197W but has a lower X-ray luminosity. The superposition of the two groups artificially enhances the apparent optical richness of the system.

4.2. Surface Brightness Distribution

We fit a β model (Cavaliere & Fusco-Femiano 1976) convolved with the PSPC PSF to the observed surface brightness of A2197W in the PSPC observation. We find a core radius $r_c = 0'.21 = 11 h^{-1}\text{kpc}$ and $\beta_X = 0.41$. Note that A2197E is $28'$ off-axis, the PSF of the PSPC at this radius is $\sim 1'$ and is anisotropic. Because of these issues, we do not attempt to fit the surface brightness profile of A2197E. Our results agree with Muriel et al. (1996).

4.3. ICM Temperature

ASCA's broad energy band (0.5-10.0 keV) is particularly useful for determining cluster temperatures. Because of the poor angular resolution of *ASCA*, we determine the emission weighted average temperature within $11'$, or $\sim 0.3 h^{-1}\text{Mpc}$; outside this radius the cluster emission is overwhelmed by the background. We obtained the screened data from Goddard Space Flight Center (GSFC). We extract a spectrum including all photons within a circle of radius $11'$ (44 pixels) centered on the cluster center for GIS data from long observations of A2197W and A2197E (Table 4). The centroid of the SIS images agree with the positions of the *ROSAT* centroids within the $\sim 0'.4$ uncertainty in the SIS position (Gotthelf 1996)¹².

¹²Available at <http://heasarc.gsfc.nasa.gov/docs/asca/newsletters/Contents4.html>

Using XSPEC (v10.0), we fit the cluster spectrum to a model including absorption (‘wabs’) parameterized by the column density of hydrogen (which we set to the Galactic value) and the standard Raymond-Smith model (Raymond & Smith 1977) characterized by temperature, iron abundance, redshift, and a normalization factor. The iron abundance is measured relative to cosmic abundance. We fit the temperature, iron abundance, and normalization as free parameters. Because we are interested in the emission-weighted X-ray temperature, we use only the GIS data because the SIS field of view does not contain the entire X-ray emitting regions.

We use the weighting system developed by Churazov et al. (1996), which properly accounts for errors in small-number statistics. Because there are few counts above 8.0 keV and the calibration uncertainties become large at low energies, we include only data from 0.8 → 8.0 keV. We fit the spectrum to slightly different ranges to ensure that the fitted model parameters are consistent for different choices.

We obtain acceptable fits by assuming that the gas is isothermal. More complicated models are thus unnecessary. Our best-fit model for A2197W has an ICM temperature of $1.55_{-0.20}^{+0.16}$ keV with an iron abundance $0.13_{-0.10}^{+0.17}$ cosmic. For A2197E, we find $kT=0.96_{-0.08}^{+0.07}$ keV and an iron abundance $0.20_{-0.05}^{+0.10}$ cosmic. Uncertainties are 90% confidence limits for one parameter and do not include calibration uncertainties. The acceptable isothermal model fits are consistent with no large temperature variations within either A2197W or A2197E, suggesting an absence of shock fronts which should be present if the groups were in the process of merging. Figure 9 (10) shows the X-ray spectrum and the best-fit model for A2197W (A2197E). These temperatures are slightly smaller but consistent with those in Finoguenov et al. (2001a) estimated from *ASCA* SIS data for the central regions of the clusters.

Using the best-fit model, we calculate a bolometric flux of $5.1(4.3) \times 10^{-12}$ ergs cm⁻² s⁻¹ for A2197W (A2197E). We calculate a bolometric luminosity of $5.3(4.5) \times 10^{42} h^{-2}$ ergs s⁻¹. If we use the *ASCA* temperatures and abundances and the *ROSAT* PSPC count rates from the pointed observations, we estimate bolometric luminosities of $5.0(4.3) \times 10^{42} h^{-2}$ ergs s⁻¹, in good agreement with the *ASCA* estimates.

4.4. Mass Estimates for A2197W and A2197E

The mass-temperature relation (Horner et al. 1999; Nevalainen et al. 2000; Finoguenov et al. 2001b) gives a straightforward estimate of the mass of a cluster given its temperature. Finoguenov et al. (2001b) find a relation of $M_{500} = (1.87 \pm 0.14) \times 10^{13} T_{keV}^{1.64 \pm 0.04} h^{-1} M_{\odot}$,

where M_{500} is the enclosed mass within a radius r_{500} inside which the mean density is 500 times the critical density and T_{keV} is the electron temperature in keV. Using $T_{keV}=4.5$ (MVFS) for A2199, the values of M_{500} for A2199, A2197W, and A2197E are 22.0, 3.8, and 1.7 respectively (in units of $10^{13}h^{-1}M_{\odot}$). Thus, the mass of A2199 is ≈ 4 times larger than the combined masses of A2197W and A2197E. The A2199 system is therefore similar to the systems considered in §2 so we are justified in applying the caustic technique to A2199.

With the assumptions of hydrostatic equilibrium, negligible non-thermal pressure, and spherical symmetry, the gravitational mass inside a radius r is

$$M_{tot}(< r) = -\frac{kT}{\mu m_p G} \left(\frac{d \ln \rho_{gas}}{d \ln r} + \frac{d \ln T}{d \ln r} \right) r \quad (4)$$

(Fabricant et al. 1980). For a uniform temperature distribution, the second term on the right hand side vanishes. We then only need to determine the gas temperature and the density distribution of the gas to calculate the gravitational mass. Under the standard hydrostatic-isothermal β_x model, the mass is related to β_x and a by

$$M_{tot}(< r) = \frac{3kT\beta_x r^3}{\mu m_p G a^2 (1 + (\frac{r}{a})^2)} = 5.65 \times 10^{13} \beta_x T_{keV} \frac{r^3}{a^2 + r^2} h^{-1} M_{\odot} \quad (5)$$

where $M_{tot}(< r)$ is the total gravitational mass within a radius r and the numerical approximation is valid for T_{keV} in keV and r and a in h^{-1} Mpc.

We use Equation 4 to calculate the total mass of A2197W within $0.5 h^{-1}$ Mpc; the estimate outside $\sim 0.3 h^{-1}$ Mpc is an extrapolation. We find a mass of $M \approx 2.2$ and $3.6 \times 10^{13} h^{-1}M_{\odot}$ at $r = 0.3$ and $0.5 h^{-1}$ Mpc respectively. White et al. (1997) use spherical deprojection to estimate $M \approx 3.9 \times 10^{13} h^{-1}M_{\odot}$ at $r = 0.28 h^{-1}$ Mpc for A2197W, in reasonable agreement with our results.

We calculate the virial mass of A2197 from galaxies within $1.5 h^{-1}$ Mpc of the X-ray peak of A2197W. We find $M_{vir} = 5.4 \times 10^{14} h^{-1}M_{\odot}$, significantly larger than the X-ray mass extrapolated assuming an isothermal sphere. Girardi et al. (1998) similarly find that the virial mass of A2197 is larger than the X-ray mass. This discrepancy is easily understood with the recognition that A2197 is the superposition of at least two groups. Supercluster galaxies not contained in the groups may further contribute to an artificially large observed velocity dispersion and hence virial mass. The calculated virial mass for A2197 is therefore meaningless.

5. Defining the Infall Region with Caustics

Figure 11 displays the redshifts of galaxies surrounding A2199 as a function of projected radius. The A2199 supercluster is located within the Great Wall (Geller & Huchra 1989, Figure 6b of Falco et al. 1999), which may complicate the interpretation of the dynamics of the system. The expected caustic pattern is easily visible. The caustic diagram of A2199 shows fewer interlopers than in the simulated superclusters, perhaps due to the galaxy formation recipe used in the simulations or perhaps due to lower infall rates such as would be present in a cosmology with $\Omega_m < 0.3$.

We perform a hierarchical structure analysis to locate the centroid of the largest system in the supercluster (D99). This analysis yields a position for A2199 of $\alpha = 16^h28^m47^s.0$, $\delta = 39^\circ30'22''$ (J2000) and $cz = 9156 \text{ km s}^{-1}$. This position is $3'.1 = 80 h^{-1}\text{kpc}$ SE of the X-ray peak.

Rines et al. (2001b) showed that the sky positions of galaxies in the infall region reveal several groups in addition to the main cluster. Figure 6 displays X-ray intensity from the RASS with contours of the local galaxy density overlaid. We calculate the galaxy density contours from cluster members (see definition in §5.7). Extended X-ray emission usually comes from an intragroup medium and thus confirms that many, but not all, of the systems are bound. NRGs395, NRGs399, and NRGs400 are X-ray faint ($L_X < 10^{42} h^{-2} \text{ergs s}^{-1}$) and thus may not be bound systems; we drop these from further analysis. Table 5 lists the coordinates and basic properties of the bound systems (see also MBGR). We calculate redshift centers cz and projected velocity dispersions σ_p according to Danese et al. (1980) for galaxies within $1.5 h^{-1}\text{Mpc}$ of the X-ray positions. Table 5 lists these properties and the number $N_{3\sigma_p}$ of member galaxies (within $\pm 3\sigma$ of the central redshift) from which they are calculated. Note that the mean redshift of A2199 is consistent with the hierarchical center, which we use in all other analyses. A2197W and A2197E overlap both on the sky and in redshift space (see §4). We caution the reader that the calculated values of σ_p for the groups may be unreliable estimates of their dynamical properties (see §6.1).

The region around NGC 6159 shows a density enhancement in both X-rays and galaxy density (visible in Figure 2 of Rines et al. 2001b, but not discussed there); A2192, a background cluster, lies immediately to the West. Trinchieri & Pietsch (2000) discuss a deep HRI observation of NGC 6159 (targeted for its unusually high ratio of X-ray to optical flux); the emission is extended. They suggest that the emission is intragroup emission but they lack the redshift information necessary to confirm this suggestion. Our redshift data show that an optical group is indeed centered on NGC 6159 and contains as many as 13 members, 7 of which are within $0.5 h^{-1}\text{Mpc}$ (Table 5).

The X-ray emission from A2199 is quite symmetric relative to other clusters (Mohr et al. 1995, MVFS), suggesting that the inner region of A2199 has not undergone any recent major mergers. The bound systems are all located at projected radii significantly larger than the virial radius ($r_v \approx 1.6 h^{-1}\text{Mpc}$, see §5.6). We identify galaxies within $1.5 h^{-1}\text{Mpc}$ of the bound systems in Figure 11. NRGs385, NRGs388, and A2199 are roughly colinear, and the galaxy contours of A2199 are noticeably elongated along this axis (Figure 6). This alignment may be coincidental or it may indicate the presence of a filament of galaxies and/or dark matter (see Rines et al. 2001b, for further discussion).

We next investigate the robustness of the infall mass profile with respect to variations in the D99 prescription.

5.1. Choice of Smoothing Parameter

The smoothing parameter q defines the width of the smoothing kernel in angular distance to the smoothing length in redshift. There is no simple *a priori* definition for this parameter. It is thus important to quantify the systematic uncertainty due to this choice (e.g., Rines et al. 2000, 2001a). D99 showed that the choice $q=25$ yields accurate mass profiles for simulated clusters; the choices $q=10$ and $q=50$ yield similar results. RQCM find that $q=5$ yields a mass profile for the Shapley Supercluster consistent with the sum of the X-ray masses of the individual systems.

Figure 12 displays the mass profile estimated from the caustics for the choices $q=10$, 25, and 50. The profiles show excellent agreement within $4 h^{-1}\text{Mpc}$, indicating that our results do not depend strongly on the choice of this parameter. Outside $4 h^{-1}\text{Mpc}$, the caustics have negligible amplitude due to the constraint on the first derivative of the caustics (see D99 and §5.3). We adopt the $q=25$ mass profile as the standard profile to test other variations.

5.2. Defining the Velocity Center of the Supercluster

In the simplest case, the velocity center of the largest system in a supercluster (in this case, A2199) is equal to the velocity center of the entire supercluster. However, clusters within a particular supercluster may have substantial peculiar velocities (Bahcall et al. 1994).

Lucey et al. (1997) estimate that the Hubble velocity with respect to the CMB at the distance of A2199 is $cz_{CMB} = 9190 \pm 360 \text{ km s}^{-1}$ using the Fundamental Plane and $9550 \pm 400 \text{ km s}^{-1}$ using $D_V - \sigma$. Using the same data, Hudson et al. (1997) and Gibbons et al. (2001) estimate $9289 \pm 307 \text{ km s}^{-1}$ and $9452 \pm 353 \text{ km s}^{-1}$ respectively. The EFAR

survey (Colless et al. 2001) reports $cz_{CMB} = 9483 \pm 741 \text{ km s}^{-1}$ using the Fundamental Plane. Giovanelli et al. (1998) use the Tully-Fisher relation to estimate $cz_{CMB} = 9231 \pm 674 \text{ km s}^{-1}$. The IR SBF study of Jensen et al. (2001) suggests $cz_{CMB} = 9302 \pm 500 \text{ km s}^{-1}$ for NGC 6166, the cD galaxy of A2199. The weighted mean yields $cz_{CMB} = 9349 \pm 157 \text{ km s}^{-1}$ for the Hubble velocity at the distance of A2199, compared to $cz_{CMB} = cz_{\odot} + 26 \text{ km s}^{-1} = 9182 \text{ km s}^{-1}$ from our hierarchical center. These results suggest that A2199 does not have a significant peculiar velocity with respect to the CMB.

The systemic redshift cz_{sup} of the supercluster is between 9000 and 9500 km s^{-1} . The central cluster A2199 appears to lie at a slightly lower redshift than the Great Wall. This offset could mean that (1) A2199 has a significant peculiar velocity with respect to the centroid of the supercluster potential or (2) the large-scale structure of the Great Wall populates only the back side of the infall region. In case (1), the redshift center of the supercluster potential is likely the redshift center of the Great Wall near A2199. In case (2), however, the supercluster potential is centered on A2199.

Because the mass profile depends on the squared amplitude of the caustics, a small shift in the systemic redshift could produce a large change in the inferred mass profile. Figures 13 and 14 show the caustics and resulting mass profiles calculated using $cz_{sup} = 9000, 9156,$ and 9500 km s^{-1} as the redshift center of the system and smoothing parameter $q = 25$. The mass profiles for $cz_{sup} = 9000$ and 9156 km s^{-1} are in excellent agreement; the mass inferred for $cz_{sup} = 9500 \text{ km s}^{-1}$ is somewhat larger outside $\approx 3 h^{-1} \text{Mpc}$, but the uncertainties are correspondingly larger. Thus, the uncertainty in cz_{sup} introduces $\lesssim 30\%$ uncertainty in the mass within $3 h^{-1} \text{Mpc}$; outside this radius, the systematic uncertainty introduced is at most a factor of 2. These uncertainties are comparable with the intrinsic systematic uncertainties estimated by D99 for isolated systems.

The X-ray group NRGs385 is located within the supercluster caustics only for $cz_{sup} = 9500 \text{ km s}^{-1}$, which is the only variation which yields a significant caustic amplitude outside $4 h^{-1} \text{Mpc}$. Indeed, if one were to sketch the locations of the caustics by eye, one would likely include the envelope of galaxies outside $4 h^{-1} \text{Mpc}$. This mass profile gives a good estimate of the upper bound on the total supercluster mass. At the largest radii sampled, the $cz_{sup} = 9500 \text{ km s}^{-1}$ mass profile yields a total mass of $10^{15} h^{-1} M_{\odot}$, roughly twice the estimates of total supercluster mass within $10 h^{-1} \text{Mpc}$ for the standard profile. The supercluster mass within $8 - 10 h^{-1} \text{Mpc}$ is thus more uncertain than the mass within $3 - 4 h^{-1} \text{Mpc}$.

5.3. Relaxing the Rules for Determining $\mathcal{A}(R_p)$

To reduce contamination from interloper galaxies, the method of D99 requires that $d\ln\mathcal{A}(r)/d\ln r < 1$. If $d\ln\mathcal{A}(r)/d\ln r > 1$, $\mathcal{A}(R_p)$ is replaced with a value such that $d\ln\mathcal{A}(r)/d\ln r = 1$. Qualitatively, this step prevents the caustics from “flaring out” with radius. This property is satisfied by all mass profiles with density profiles decreasing as $\rho \propto r^{-\alpha}$ at large radii for $\alpha \geq 2$ (all the models considered in §2.1 satisfy this requirement). This requirement may introduce a bias into the final mass profile. Figure 15 shows the shape of the caustics calculated without this requirement and without requiring that the caustics be symmetric (i.e., the amplitudes of the upper and lower caustics are independent). Rines et al. (2001b) use this variation. Figure 16 shows the mass profile calculated from these caustics using the minimum caustic amplitude at each radius for $q = 25$ and $cz_{sup} = 9156 \text{ km s}^{-1}$. Within $4 h^{-1}\text{Mpc}$, the mass profile calculated in this manner is nearly identical to the standard profile. Outside $4 h^{-1}\text{Mpc}$, the mass profile lies between the standard profile and that calculated with $cz_{sup} = 9500 \text{ km s}^{-1}$.

5.4. Substructure and Caustics

In A2199, we directly see the substructure which disrupts the sharp caustic pattern expected for simple spherical infall (Kaiser 1987). The location of subclusters within the caustic pattern of A2199 demonstrates that they are falling into the supercluster. We split the entire region into two halves along a line passing through A2199 to test the importance of A2197 in determining the location of the caustics. The caustics at the radius of A2197 have a larger amplitude towards A2197 than away from it (Figure 17). There is a noticeable deficit of galaxies at the radial distance of A2197 on the opposite side of A2199. However, the caustics away from A2197 in the vicinity of NRGs388 appear similar to those towards A2197, although the estimator yields a smaller amplitude due to the deficit of galaxies at smaller radii and the constraint that the caustics not rise too quickly. We discuss the interplay of group and supercluster dynamics in §6. Figure 18 shows the mass profiles calculated towards and away A2197; the two profiles agree within uncertainties.

5.5. Comparison to Model Mass Profiles

We fit the mass profile to the models discussed in §2.1. Table 7 lists the best-fit parameters a (fixed for SIS) and $M(a)$ for the three models for the variations in q , cz_{sup} , and fitting technique described above. The fits only include radii with $\mathcal{A}(r) > 100 \text{ km s}^{-1}$. Because

the data points in the mass profile are not independent, the absolute values of χ_v^2 listed in Table 7 are only indicative, but it is clear that, as for the simulated superclusters, the NFW and Hernquist profiles provide acceptable fits to the infall mass profile while the SIS is excluded for all variations. The NFW profile generally provides a better fit to the data than the Hernquist profile. The parameters of the best-fit mass profile are quite robust with respect to the variations in the estimator discussed above. As noted in §4.2, the mass profile calculated assuming $cz_{sup} = 9500 \text{ km s}^{-1}$ yields a significantly larger total mass than the other estimates, but the mass profile inside $3 h^{-1}\text{Mpc}$ is very similar to the others.

For the standard mass profile, the best-fit NFW parameters are $\log \delta_c = 4.4$, concentration $c = r_{200}/a = 8$, and $M_{200} = 3.2 \times 10^{14} = 7.8M_*$ for the NFW definition of M_* in a ΛCDM model ($M_{200} = 20M_*$ for the SCDM model in NFW). Our results match the predicted $\delta_c - M_{200}$ relation for most of the cosmological models in NFW.

5.6. Comparison to Other Mass Estimates

MVFS use *ROSAT* X-ray images and spatially-resolved spectroscopy from *ASCA* to estimate the mass profile of A2199 in the range $0.1 - 0.6 h^{-1}\text{Mpc}$. This mass profile is one of the few X-ray cluster mass profiles measured to such a large radius with a resolved temperature profile. The X-ray mass profile, which is completely independent of the caustic technique, shows excellent agreement with the standard profile (Figure 19). Figure 19 also shows a mass estimate from deprojecting *Einstein* data (White et al. 1997) and the best-fit NFW profile to the deprojected *Chandra* data at small scales (Johnstone et al. 2002, however, note that this NFW profile is formally rejected by the data). The standard mass profile agrees well with the former but not with the latter. The ICM is far from hydrostatic equilibrium in the core of A2199, so the mass estimate at these small radii is perhaps not reliable.

We use the prescription of Girardi et al. (1998) to estimate a virial radius $r_v = 1.6 h^{-1}\text{Mpc}$ for A2199. We estimate the virial mass of A2199 using all galaxies inside the caustics and within r_v . The virial mass is $5.34 \times 10^{14} h^{-1} M_\odot$, in good agreement with Girardi et al. (1998). The standard profile yields a mass about 30% smaller than this value at r_v . This difference is within the uncertainty range expected for the caustic technique.

5.7. Velocity Dispersion Profile

As a final consistency check of the caustic mass profile, we calculate the velocity dispersion as a function of radius in bins of 25 galaxies. For this calculation, we include all galaxies inside the caustics of either the standard caustics or the caustics calculated with $cz_{sup} = 9500 \text{ km s}^{-1}$. Including only galaxies in the former caustics yields similar results within $4 h^{-1}\text{Mpc}$; very few galaxies are classified as members beyond this radius. Figure 20 displays both the regular and the integrated velocity dispersion profiles along with the predicted profiles based on the best-fit Hernquist and NFW mass profiles and an assumption of isotropic orbits. The predicted profiles match the observed profiles quite well, and thus the galaxy orbits in A2199 are consistent with isotropic. Note that, as in A576, the integrated velocity dispersion decreases smoothly with radius and does not reach an asymptotic value which could be easily interpreted as the velocity dispersion of the cluster.

6. Discussion

Projection effects introduce the largest uncertainty in the caustic technique both for isolated clusters and simple superclusters (D99). The X-ray masses for A2197W and A2197E are factors of 6 and 13 smaller than A2199. Tests of similar systems from simulations indicate that the caustic technique should yield an accurate mass profile for the supercluster. The uncertainty in the redshift center of the supercluster results in a factor of two uncertainty in the total supercluster mass within 8-10 $h^{-1}\text{Mpc}$. Within 3 $h^{-1}\text{Mpc}$, however, we estimate the error on the enclosed mass to be only about 30%, comparable to the intrinsic uncertainty estimated by simulations.

6.1. Do Supercluster Dynamics Dominate Group Dynamics?

At the projected radii of A2197W and A2197E, the inferred group masses are a small fraction of the enclosed supercluster mass. The supercluster dynamics may dominate the observed dynamics of groups in the infall region. The supercluster may increase the velocity dispersion of the groups either directly or by introducing interlopers which are bound to the supercluster but are not group members.

One test of the relative importance of group and supercluster dynamics is to predict the velocity dispersion of the groups from their X-ray luminosities or temperatures and the $L_X - \sigma$ or $\sigma - T_X$ relation (Xue & Wu 2000, MBGR and references therein). We list the predicted and observed velocity dispersions in Table 8. Except for A2199 and the NGC 6159

group, the observed velocity dispersions are larger than those predicted by the $L_X - \sigma$ or the $\sigma - T_X$ relation, suggesting that the observed dynamics of the groups are dominated by the supercluster, either physically (e.g., due to tidal forces from filaments) or observationally due to the increased density of interlopers.

At the radii of A2197, NRGs388, and NGC 6159, the amplitude of the caustics is relatively unaffected by the presence of these subsystems. At the projected distance of NRGs385, however, the caustic pattern (Figure 15) and the velocity dispersion profile (Figure 20) shows a larger amplitude than at smaller radii. This result shows that the caustic amplitude is strongly affected by substructure at this radius. The redshift center of the supercluster determines whether NRGs385 is inside the supercluster caustics.

6.2. X-ray Contribution of Radio Sources

X-ray emission from radio sources can contribute significantly to the total X-ray luminosity of a galaxy group. Indeed, Feretti et al. (1995) find that both NRGs385 and NRGs388 contain radio galaxies which are detected in X-rays. From *ROSAT* PSPC data, they find that NGC 6107 and NGC 6109 contain 6% and 1.8% respectively of the total X-ray luminosity of NRGs385. For NRGs388, they suggest that the observed X-ray luminosity is entirely associated with the halo of NGC 6137 and not with an intragroup medium. Reliable estimates of σ_p from the $L_X - \sigma_p$ relation therefore require pointed X-ray observations of groups to determine the X-ray luminosity due to the intragroup medium.

6.3. Are the Groups Really Infalling?

The location of the groups within the caustics indicates that they are dynamically linked to the A2199 supercluster. This connection, however, does not necessarily imply that the groups are currently infalling onto the supercluster. The turnaround radius r_{ta} for a $\Lambda = 0$ universe satisfies $\rho_m(< r_{ta}) = \Omega_m \rho_c (1 + \Delta_{0,turn})$ where ρ_c is the critical density and $\Delta_{0,turn}$ is given by Equation 8 in Regös & Geller (1989). In the limit $\Omega_m = 1$, $\rho_m(< r_{ta}) = (9\pi^2/16)\rho_c$. The standard mass profile yields $r_{ta} \approx 4.5-5.7 h^{-1}\text{Mpc}$ for $\Omega_m = 1 \rightarrow 0.025$ where we take a lower limit on Ω_m from the baryon density $\Omega_b h^2 = 0.025$ (Pettini & Bowen 2001) and the assumption that $h \leq 1$. For the more massive profile inferred by assuming $cz_{sup} = 9500 \text{ km s}^{-1}$, the turnaround radius for the above range of Ω_m is $r_{ta} = 5.0-6.5 h^{-1}\text{Mpc}$. The turnaround radius is smaller in the presence of a non-zero cosmological constant, but this effect is small in the present epoch for $\Lambda \lesssim 1$ (Lilje & Lahav 1991; Martel 1991). Thus,

A2197W, A2197E, and NRGs388 are in the infall region of A2199 for most combinations of geometry and cosmology (the expectation value of the deprojected radius is $\langle r \rangle = \pi R_p/2$). The NGC 6159 group is a borderline case; it is infalling for the standard mass profile and our adopted cosmology only for small angles ($\lesssim 20^\circ$) between the plane of the sky and the line connecting A2199 and NGC 6159. NRGs385 and NRGs396 are not infalling onto the supercluster. A simulation of the future evolution of the nearby universe (Nagamine & Loeb 2002) shows that some objects outside the turnaround radius of clusters in the present epoch but with large peculiar velocities may eventually become cluster members.

Based on the presence of a caustic pattern around NRGs385 and an unusual offset between its X-ray and optical peaks, we previously suggested that NRGs385 might be infalling onto A2199 (Rines et al. 2001b). We have shown here, however, that the mass profile robustly excludes this possibility. The unusual morphology of NRGs385 is probably related to the local large-scale structure and is not caused by effects related to infall (e.g., ram pressure stripping).

The caustic pattern is present beyond the turnaround radius, suggesting that the gravitational potential of a cluster (or simple supercluster) and surrounding large-scale structure can significantly affect the kinematics of objects outside the infall region. The caustics extend beyond the turnaround radius in the simulations of D99. A similar effect is seen in the galaxy-galaxy autocorrelation function (e.g., Peacock et al. 2001). The existence of large-scale structure obscures the location of the turnaround radius in the projected radius-redshift diagram.

7. Conclusions

We have previously demonstrated that the infall region of A2199 contains several bound subclusters (Rines et al. 2001b). Here, we show that, in simulations, caustics yield accurate mass profiles of superclusters dominated by a central cluster 2-6 times more massive than all other systems in the supercluster. The mass profiles of the simulated clusters agree with NFW or Hernquist models but not with a singular isothermal sphere.

X-ray data demonstrate that A2197 is the superposition of two bound X-ray groups (centered on the bright galaxies NGC 6160 and NGC 6173) which may be interacting. Because of the complexity of A2197, the virial theorem does not yield an accurate mass estimate. The X-ray masses for A2197W and A2197E are factors of 6 and 13 smaller than A2199. Tests of similar superclusters from simulations indicate that the caustic technique should yield an accurate mass profile for the A2199 supercluster.

The supercluster mass profile suffers some uncertainty due to the complexity of the surrounding large-scale structure and the resulting difficulty in determining the redshift center of the supercluster. Within $3 h^{-1}\text{Mpc}$, however, this uncertainty is no larger than the scatter predicted by numerical simulations for isolated clusters. The infall mass profile is in excellent agreement with independent X-ray estimates at small radii. At large radii, the mass profile is clearly inconsistent with an isothermal sphere but agrees with profiles motivated by simulations.

The mass profile indicates that A2197W, A2197E, and NRGs388 are bound, infalling groups; NRGs385 and NRGs396 (and the NGC 6159 group for inclination angles $\gtrsim 20^\circ$) are not infalling onto the supercluster in the present epoch. This result demonstrates that the presence of caustics at large radii from clusters does not prove that galaxies or groups within these caustics are inside the infall region. In other words, the gravitational potential of a cluster and surrounding large-scale structure can significantly affect the kinematics of objects outside the turnaround radius. The observed velocity dispersions of the groups surrounding A2199 are significantly larger than predicted by their X-ray properties and scaling relations. The observed kinematic properties of galaxy groups within and near superclusters are likely dominated by the supercluster and not by the group potential.

The caustic technique is a robust estimator of cluster mass profiles ranging in mass from Fornax to the Shapley Supercluster. We demonstrate that the technique is robust for simple superclusters, both in simulations and in observations of the A2199/A2197 supercluster. We plan to analyze a sample of 8 nearby clusters and study the mass-to-light ratio throughout the infall regions of several of these systems.

This project would not have been possible without the assistance of Perry Berlind and Michael Calkins, the remote observers at FLWO, and Susan Tokarz, who processed the spectroscopic data. KR and MJG are supported in part by the Smithsonian Institution. JJM is supported by NASA LTSA grant NAG 5-11415. The N-body simulations, halo and galaxy catalogues used in this paper are publically available at <http://www.mpa-garching.mpg.de/NumCos>. The simulations were carried out at the Computer Center of the Max-Planck Society in Garching and at the EPCC in Edinburgh, as part of the Virgo Consortium project. We also thank the Max-Planck Institut für Astrophysik where some of the computing for this work was done. The National Geographic Society - Palomar Observatory Sky Atlas (POSS-I) was made by the California Institute of Technology with grants from the National Geographic Society. This research has made use of the NASA/IPAC Extragalactic Database (NED) which is operated by the Jet Propulsion Laboratory, California Institute of Technology, under contract with the National Aeronautics and Space Administration. We thank the referee for detailed comments which improved the presentation of this paper.

REFERENCES

- Böhringer, H. et al. 2000, *ApJS*, 129, 435
- Bade, N., Fink, H. H., Engels, D., Voges, W., Hagen, H.-J., Wisotzki, L., & Reimers, D. 1995, *A&AS*, 110, 469+
- Bahcall, N. A., Gramann, M., & Cen, R. 1994, *ApJ*, 436, 23
- Butcher, H. & Oemler, A. 1984, *ApJ*, 285, 426
- Cavaliere, A. & Fusco-Femiano, R. 1976, *A&A*, 49, 137
- Churazov, E., Gilfanov, M., Forman, W., & Jones, C. 1996, *ApJ*, 471, 673
- Colless, M., Saglia, R. P., Burstein, D., Davies, R. L., McMahan, R. K., & Wegner, G. 2001, *MNRAS*, 321, 277
- Crampton, D., Cowley, A. P., Hartwick, F. D. A., & Ko, P. W. 1992, *AJ*, 104, 1706
- Danese, L., de Zotti, G., & di Tullio, G. 1980, *A&A*, 82, 322
- de Vaucouleurs, G., de Vaucouleurs, A., Corwin, J. R., Buta, R. J., Paturel, G., & Fouque, P. 1991, in *Third reference catalogue of Bright galaxies, 1991*, New York : Springer-Verlag.
- Diaferio, A. 1999, *MNRAS*, 309, 610
- Diaferio, A. & Geller, M. J. 1997, *ApJ*, 481, 633
- Drinkwater, M. J., Gregg, M. D., & Colless, M. 2001, *ApJ*, 548, L139
- Ebeling, H., Edge, A. C., Allen, S. W., Crawford, C. S., Fabian, A. C., & Huchra, J. P. 2000, *MNRAS*, 318, 333
- Ellingson, E., Lin, H., Yee, H. K. C., & Carlberg, R. G. 2001, *ApJ*, 547, 609
- Fabricant, D., Cheimets, P., Caldwell, N., & Geary, J. 1998, *PASP*, 110, 79
- Fabricant, D. & Hertz, E. 1990, in *Instrumentation in astronomy VII; Proceedings of the Meeting, Tucson, AZ, Feb. 13-17, 1990 (A91-29601 11-35)*. Bellingham, WA, Society of Photo-Optical Instrumentation Engineers, 1990, p. 747-753., Vol. 1235, 747–753
- Fabricant, D., Lecar, M., & Gorenstein, P. 1980, *ApJ*, 241, 552

- Falco, E. E. et al. 1999, *PASP*, 111, 438
- Feretti, L., Fanti, R., Parma, P., Massaglia, S., Trussoni, E., & Brinkmann, W. 1995, *A&A*, 298, 699
- Finoguenov, A., Arnaud, M., & David, L. P. 2001a, *ApJ*, 555, 191
- Finoguenov, A., Reiprich, T. H., & Böhringer, H. 2001b, *A&A*, 368, 749
- Freudling, W., Haynes, M. P., & Giovanelli, R. 1992, *ApJS*, 79, 157
- Geller, M. J., Diaferio, A., & Kurtz, M. J. 1999, *ApJ*, 517, L23
- Geller, M. J. & Huchra, J. P. 1989, *Science*, 246, 897
- Gibbons, R. A., Fruchter, A. S., & Bothun, G. D. 2001, *AJ*, 121, 649
- Giovanelli, R., Haynes, M. P., Salzer, J. J., Wegner, G., da Costa, L. N., & Freudling, W. 1998, *AJ*, 116, 2632
- Girardi, M., Giuricin, G., Mardirossian, F., Mezzetti, M., & Boschin, W. 1998, *ApJ*, 505, 74
- Gotthelf, E. 1996, in *ASCA News*, 4
- Haynes, M. P., Giovanelli, R., Herter, T., Vogt, N. P., Freudling, W., Maia, M. A. G., Salzer, J. J., & Wegner, G. 1997, *AJ*, 113, 1197
- Hernquist, L. 1990, *ApJ*, 356, 359
- Hill, J. M. & Oegerle, W. R. 1998, *AJ*, 116, 1529
- Horner, D. J., Mushotzky, R. F., & Scharf, C. A. 1999, *ApJ*, 520, 78
- Hudson, M. J., Lucey, J. R., Smith, R. J., & Steel, J. 1997, *MNRAS*, 291, 488+
- Humphreys, R. M., Landau, R., Ghigo, F. D., Zumach, W., & Labonte, A. E. 1991, *AJ*, 102, 395
- Jensen, J. B., Tonry, J. L., Thompson, R. I., Ajhar, E. A., Lauer, T. R., Rieke, M. J., Postman, M., & Liu, M. C. 2001, *ApJ*, 550, 503
- Johnstone, R. M., Allen, S. W., Fabian, A. C., & Saunders, J. S. 2002, *MNRAS*, accepted (astro-ph/0202071)
- Kaiser, N. 1987, *MNRAS*, 227, 1

- Kaiser, N., Wilson, G., Luppino, G., Kofman, L., Gioia, I., Metzger, M., & Dahle, H. 2002, ApJ, submitted (astro-ph/9809268)
- Kauffmann, G., Colberg, J. M., Diaferio, A., & White, S. D. M. 1999a, MNRAS, 303, 188
- . 1999b, MNRAS, 307, 529
- Kirshner, R. P., Oemler, A., Schechter, P. L., & Shectman, S. A. 1983, AJ, 88, 1285
- Knezek, P. M. & Bregman, J. N. 1998, AJ, 115, 1737
- Kurtz, M. J. & Mink, D. J. 1998, PASP, 110, 934
- Lilje, P. B. & Lahav, O. 1991, ApJ, 374, 29
- Lucey, J. R., Guzman, R., Steel, J., & Carter, D. 1997, MNRAS, 287, 899
- Mahdavi, A., Böhringer, H., Geller, M. J., & Ramella, M. 2000, ApJ, 534, 114
- Mahdavi, A. & Geller, M. J. 2001, ApJ, 554, L129
- Mahdavi, A., Geller, M. J., Böhringer, H., Kurtz, M. J., & Ramella, M. 1999, ApJ, 518, 69
- Markevitch, M., Vikhlinin, A., Forman, W. R., & Sarazin, C. L. 1999, ApJ, 527, 545
- Martel, H. 1991, ApJ, 377, 7
- Mohr, J. J., Evrard, A. E., Fabricant, D. G., & Geller, M. J. 1995, ApJ, 447, 8
- Mohr, J. J. & Wegner, G. 1997, AJ, 114, 25
- Muriel, H., Böhringer, H., & Voges, W. 1996, in Roentgenstrahlung from the Universe, 601–602
- Nagamine, K. & Loeb, A. 2002, ApJ, submitted (astro-ph/0204249)
- Navarro, J. F., Frenk, C. S., & White, S. D. M. 1997, ApJ, 490, 493
- Nevalainen, J., Markevitch, M., & Forman, W. 2000, ApJ, 532, 694
- Peacock, J. A. et al. 2001, Nature, 410, 169
- Pettini, M. & Bowen, D. V. 2001, ApJ, 560, 41
- Raymond, J. C. & Smith, B. W. 1977, ApJS, 35, 419
- Regös, E. & Geller, M. J. 1989, AJ, 98, 755

- Reisenegger, A., Quintana, H., Carrasco, E. R., & Maze, J. 2000, *AJ*, 120, 523
- Rines, K., Geller, M. J., Diaferio, A., Mohr, J. J., & Wegner, G. A. 2000, *AJ*, 120, 2338
- Rines, K., Geller, M. J., Kurtz, M.J.and Diaferio, A., Jarrett, T., & Huchra, J. 2001a, *ApJ*, 561, L41
- Rines, K., Mahdavi, A., Geller, M. J., Diaferio, A., Mohr, J. J., & Wegner, G. 2001b, *ApJ*, 555, 558
- Small, T. A., Ma, C., Sargent, W. L. W., & Hamilton, D. 1998, *ApJ*, 492, 45
- Strauss, M. A. & Huchra, J. 1988, *AJ*, 95, 1602
- Trinchieri, G. & Pietsch, W. 2000, *A&A*, 353, 487
- Tustin, A. W., Geller, M. J., Kenyon, S. J., & Diaferio, A. 2001, *AJ*, 122, 1289
- Vedel, H. & Hartwick, F. D. A. 1998, *ApJ*, 501, 509
- Voges, W. et al. 1999, *A&A*, 349, 389
- White, D. A., Jones, C., & Forman, W. 1997, *MNRAS*, 292, 419
- Xue, Y. & Wu, X. 2000, *ApJ*, 538, 65
- Zabludoff, A. I., Geller, M. J., Huchra, J. P., & Vogeley, M. S. 1993, *AJ*, 106, 1273

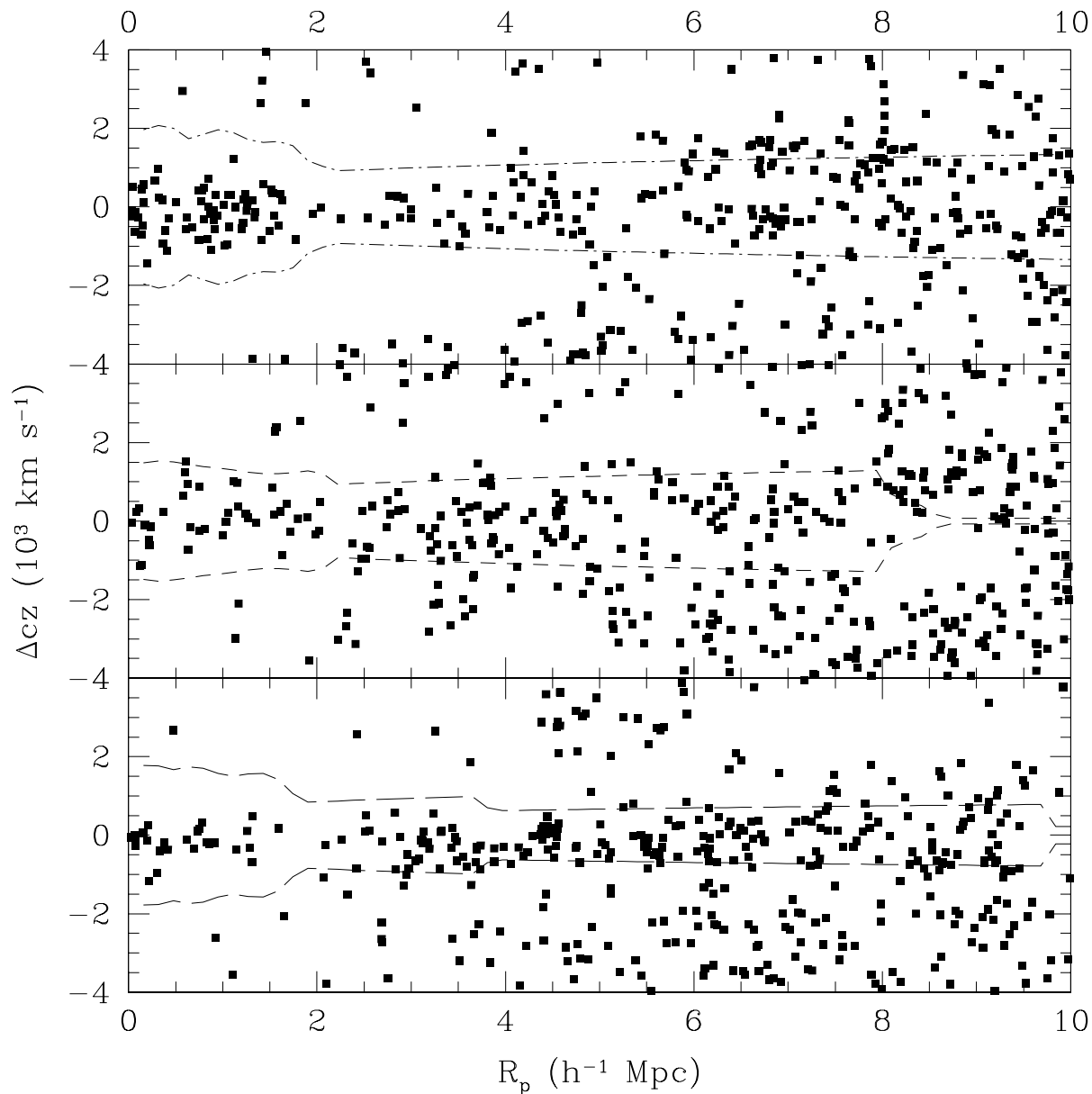


Fig. 1.— Redshift versus radius and the caustics for a simulated supercluster (ID 121) with mass ratio $M_1/M_2 = 2.0$ (see text for definition) projected along three different lines of sight. We use different line styles to enable comparison with the estimated mass profiles in Figures 4 and 5.

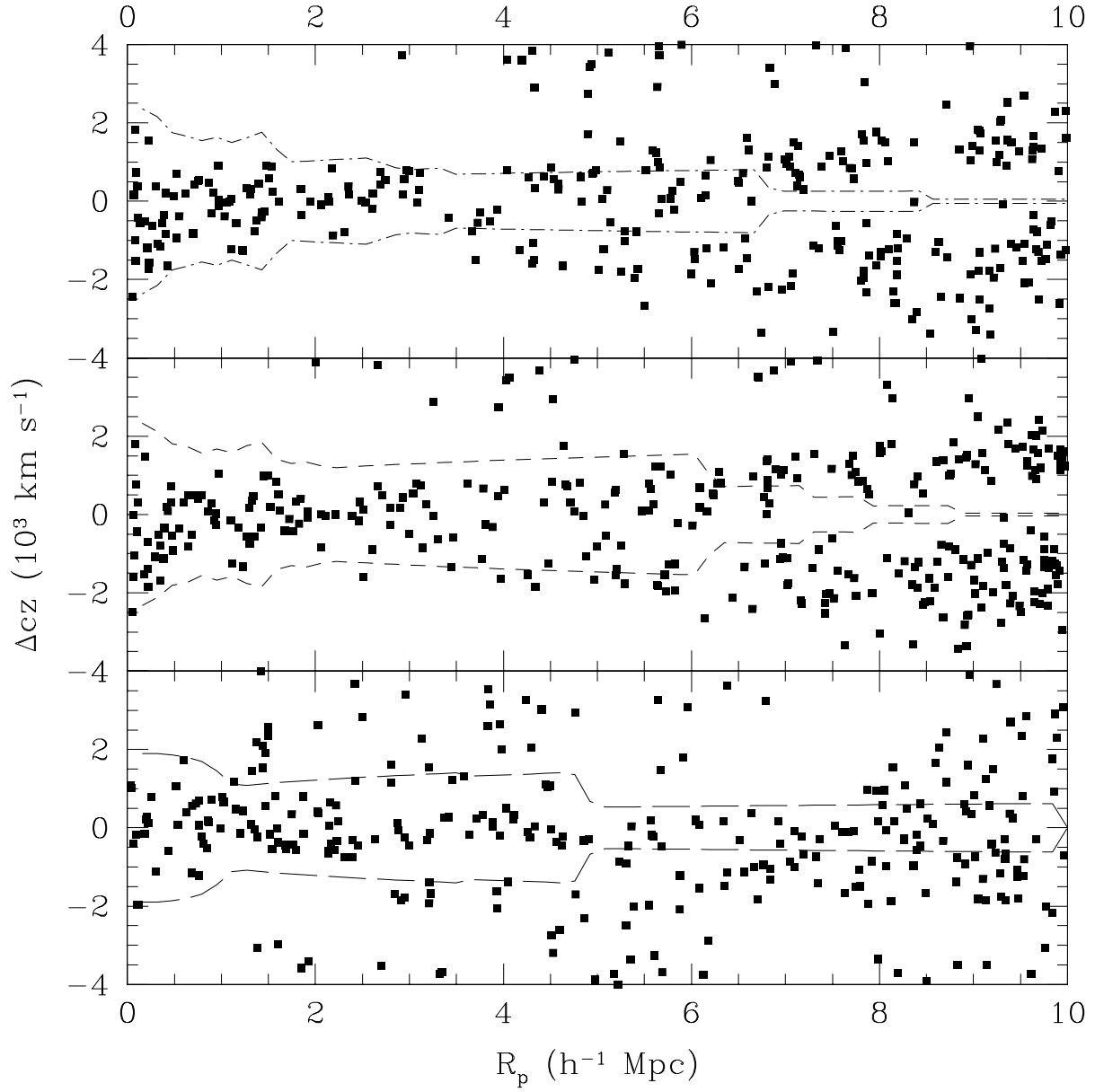


Fig. 2.— Same as Figure 1 for the simulated supercluster ID 156 with mass ratio $M_1/M_2 = 4.4$.

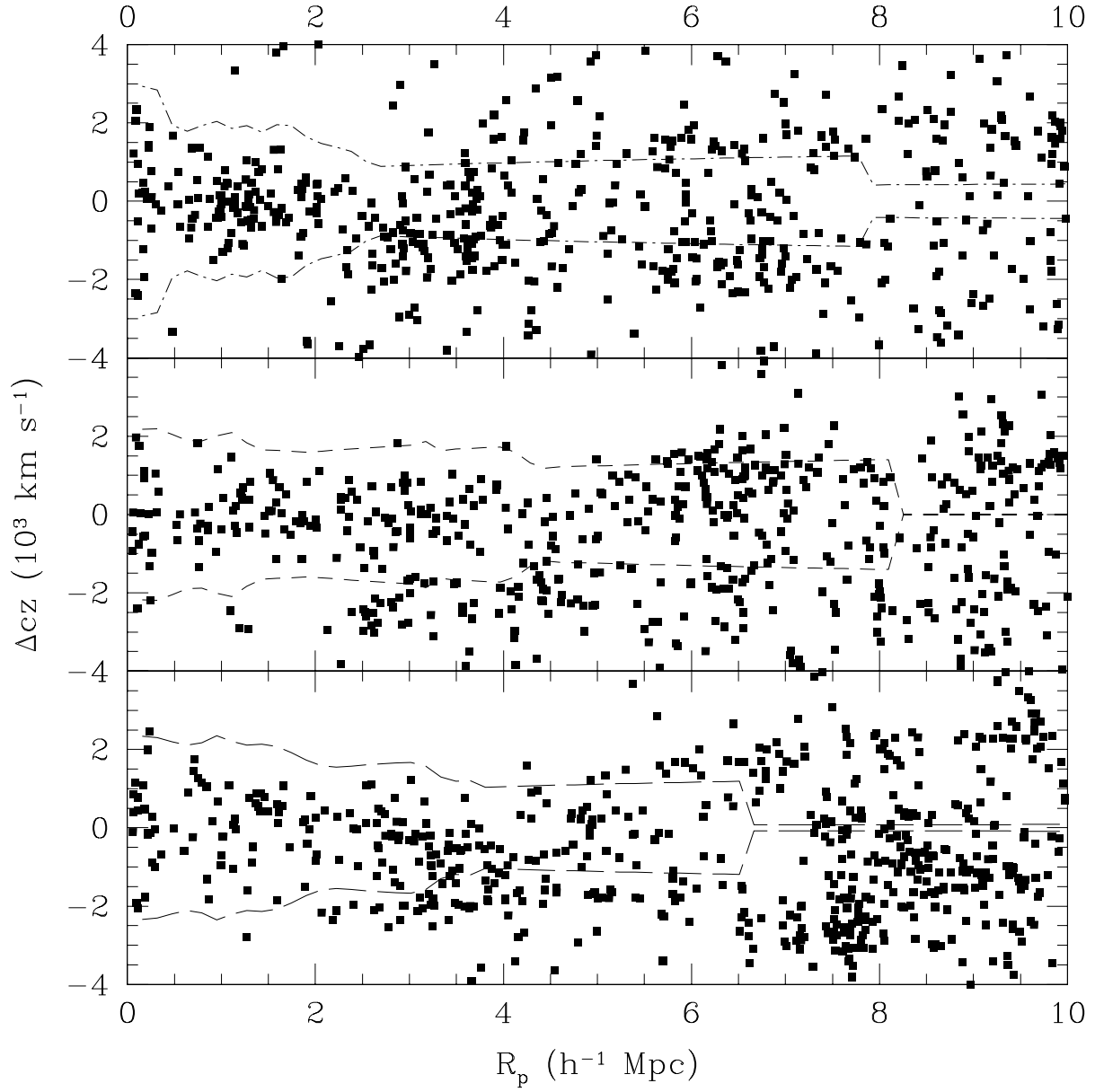


Fig. 3.— Same as Figure 1 for the simulated supercluster ID 162 with mass ratio $M_1/M_2 = 6.2$.

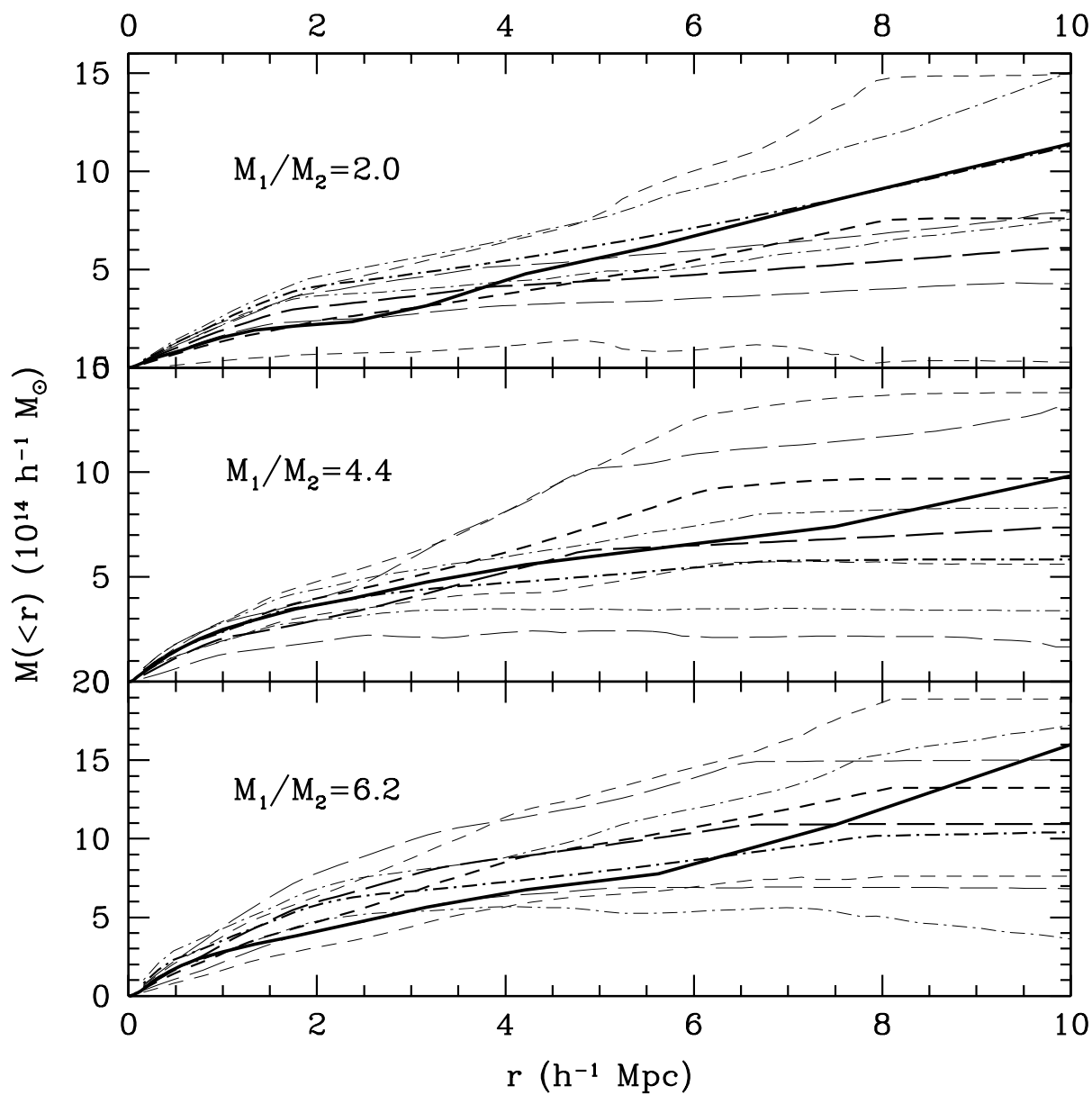


Fig. 4.— Comparison of caustic mass profiles to true mass profiles for simulated superclusters. The three sets of lines show the 1- σ ranges of the infall mass profile from three different lines of sight. The line styles are the same as in Figures 1-3.

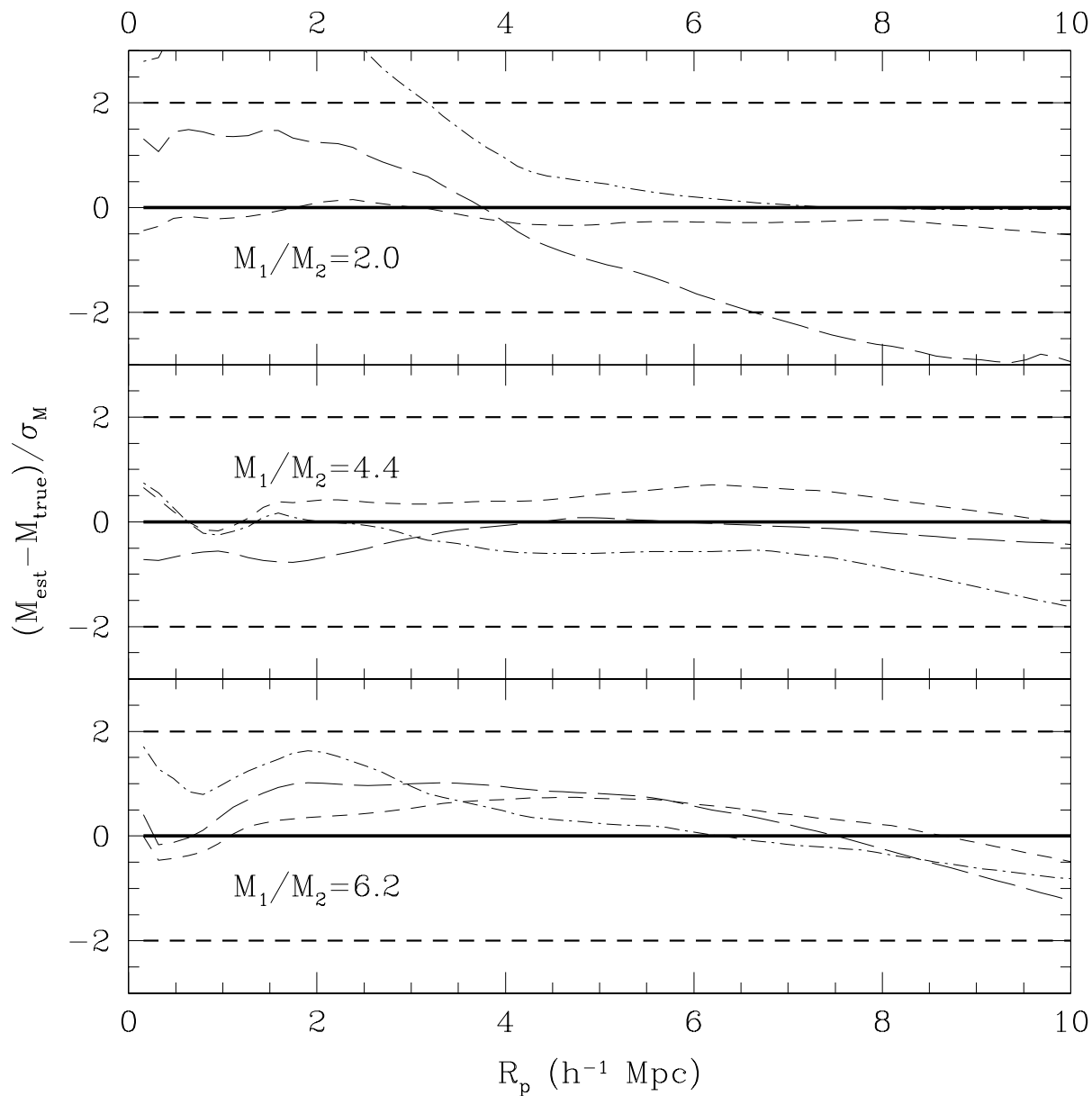


Fig. 5.— Difference between estimated and true masses of the simulated superclusters in units of the uncertainty in the estimated mass. The estimates differ by more than 2σ from the true mass profile only in the supercluster with $M_1/M_2 = 2.0$. The line styles are the same as in Figures 1-3.

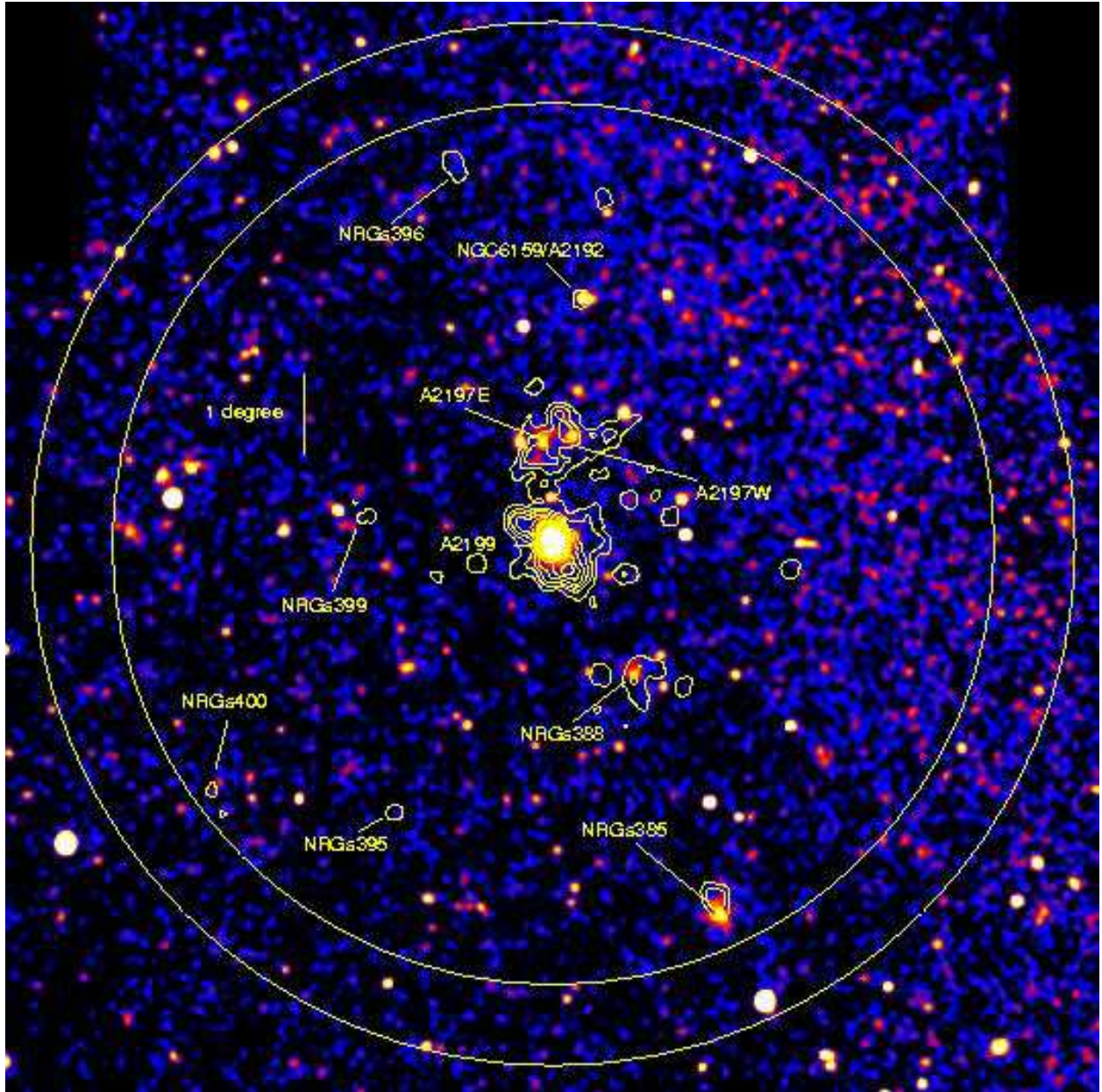


Fig. 6.— Galaxy density contours overlaid on RASS X-ray data. The RASS data have been exposure corrected. Both RASS data and the galaxy density were smoothed with a Gaussian with $2'$ FWHM. Some groups of galaxies have no associated X-ray emission detectable in the RASS. The inner circle is the limit of our redshift survey; our sample also includes galaxies with redshifts from the literature within the outer circle.

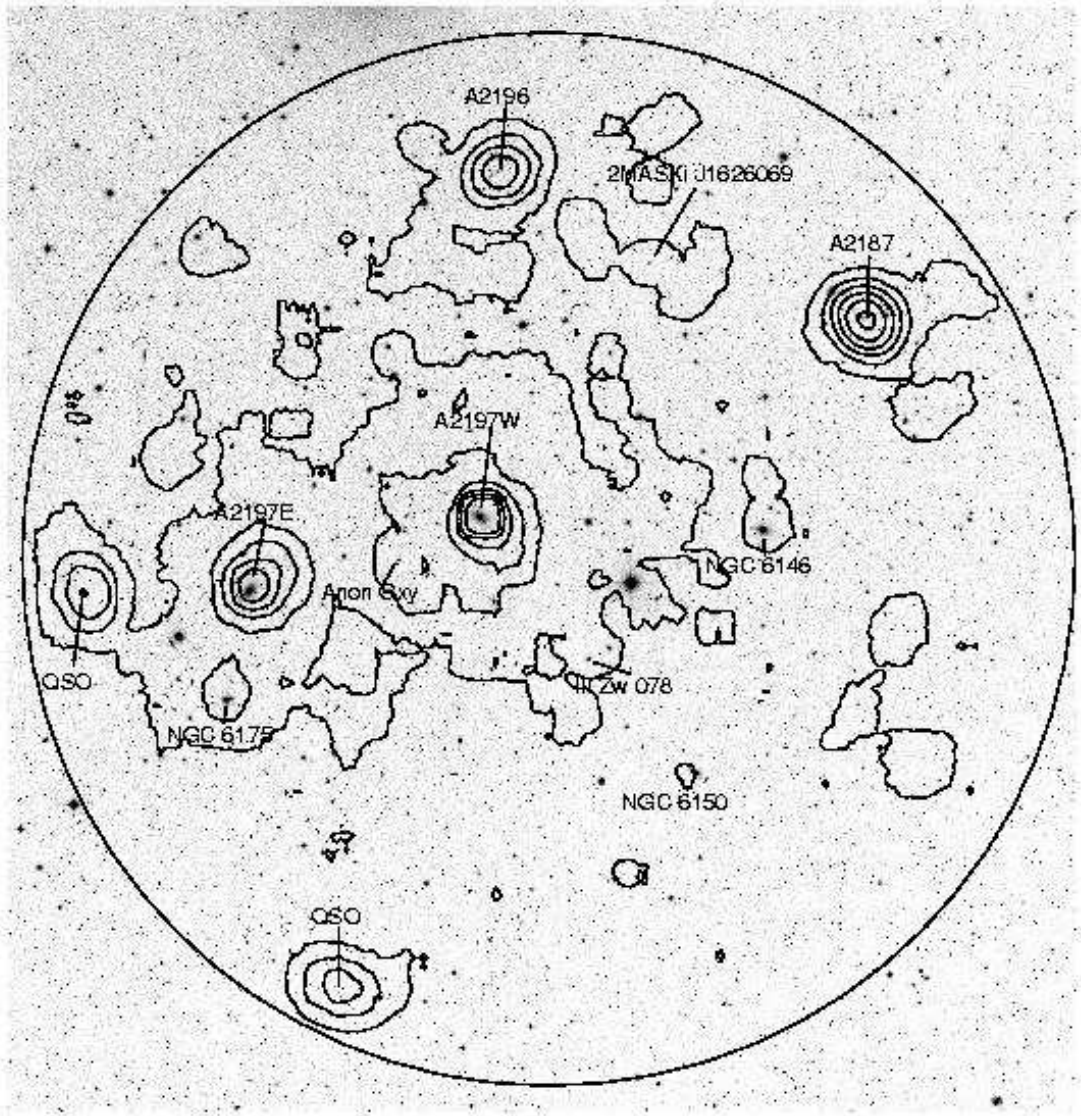


Fig. 7.— X-ray contours from a 13.5-ksec *ROSAT* PSPC observation of A2197 overlaid on optical POSS I data. The diameter of the PSPC field is 2° . North is up and East is to the left.

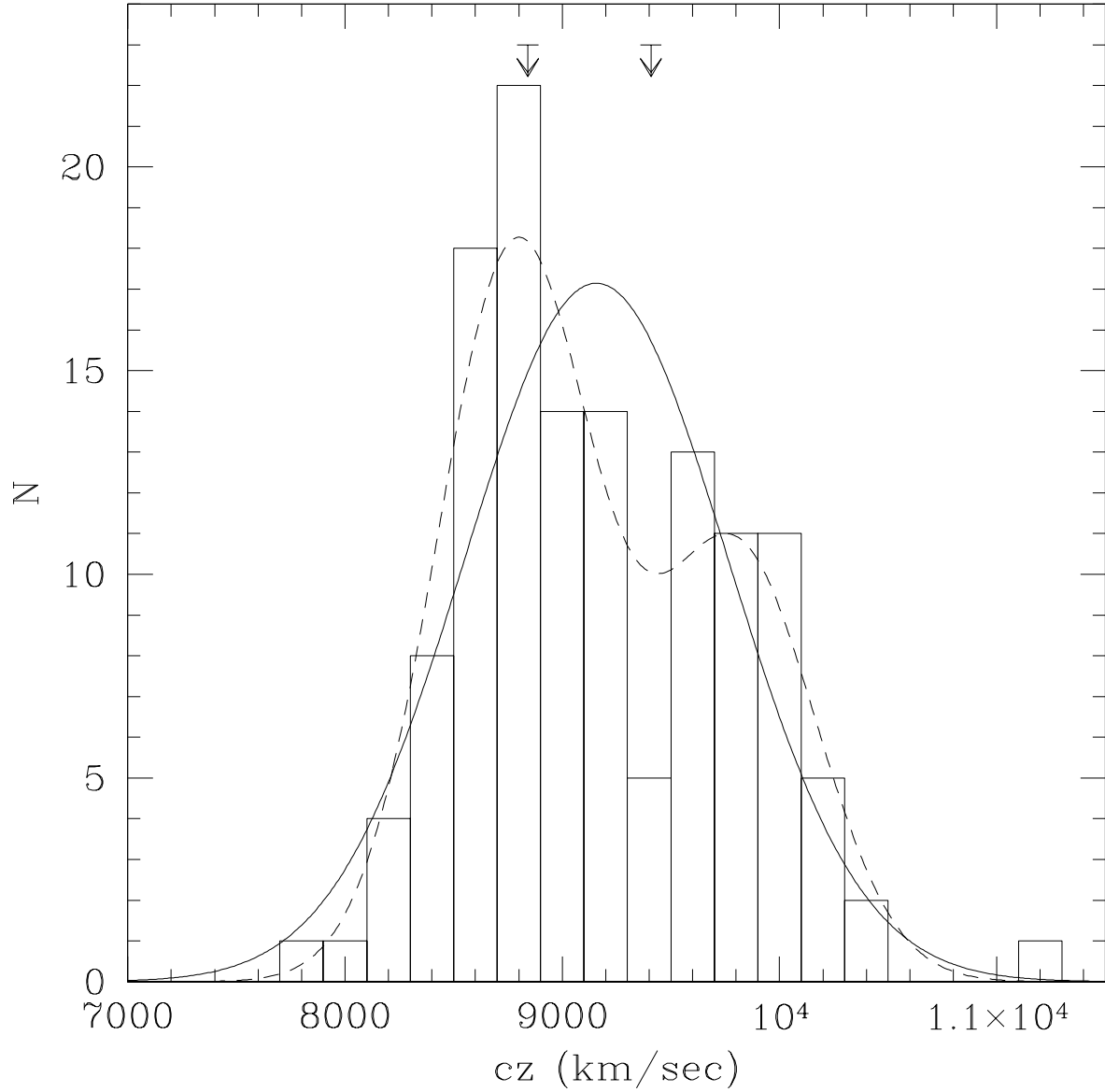
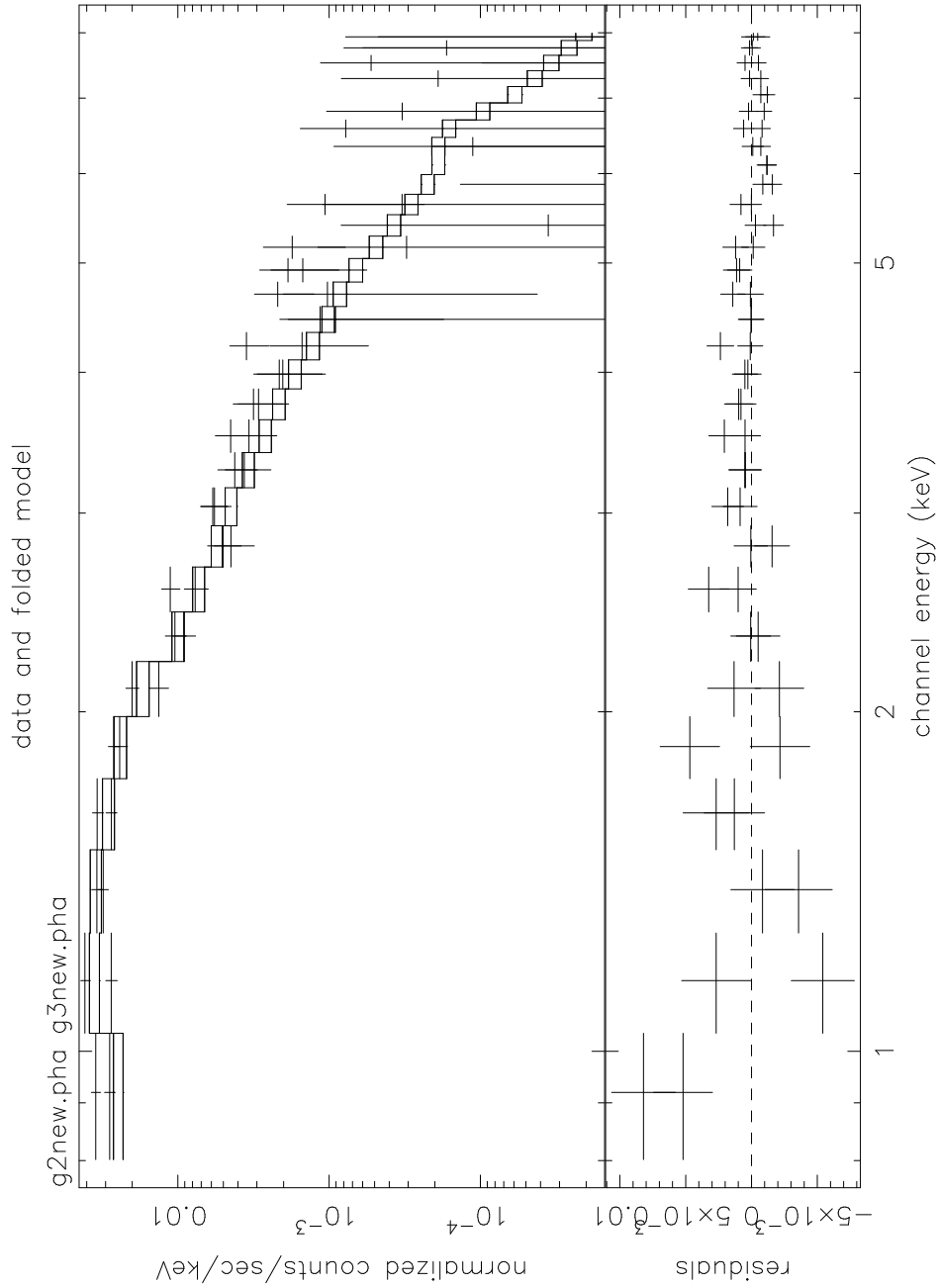


Fig. 8.— Redshift histogram of galaxies within $1.5 h^{-1}\text{Mpc}$ of A2197. The solid line shows the best-fit Gaussian and the dashed line shows a two-component model. Arrows indicate the redshifts of NGC 6173 and NGC 6160, the cD galaxies of A2197E and A2197W respectively.



krines 4-Apr-2002 18:40

Fig. 9.— *ASCA* X-ray spectrum of A2197W. The data points show the GIS 2 and GIS 3 instruments and the lines show the best-fit thermal plasma model convolved with the *ASCA* response.

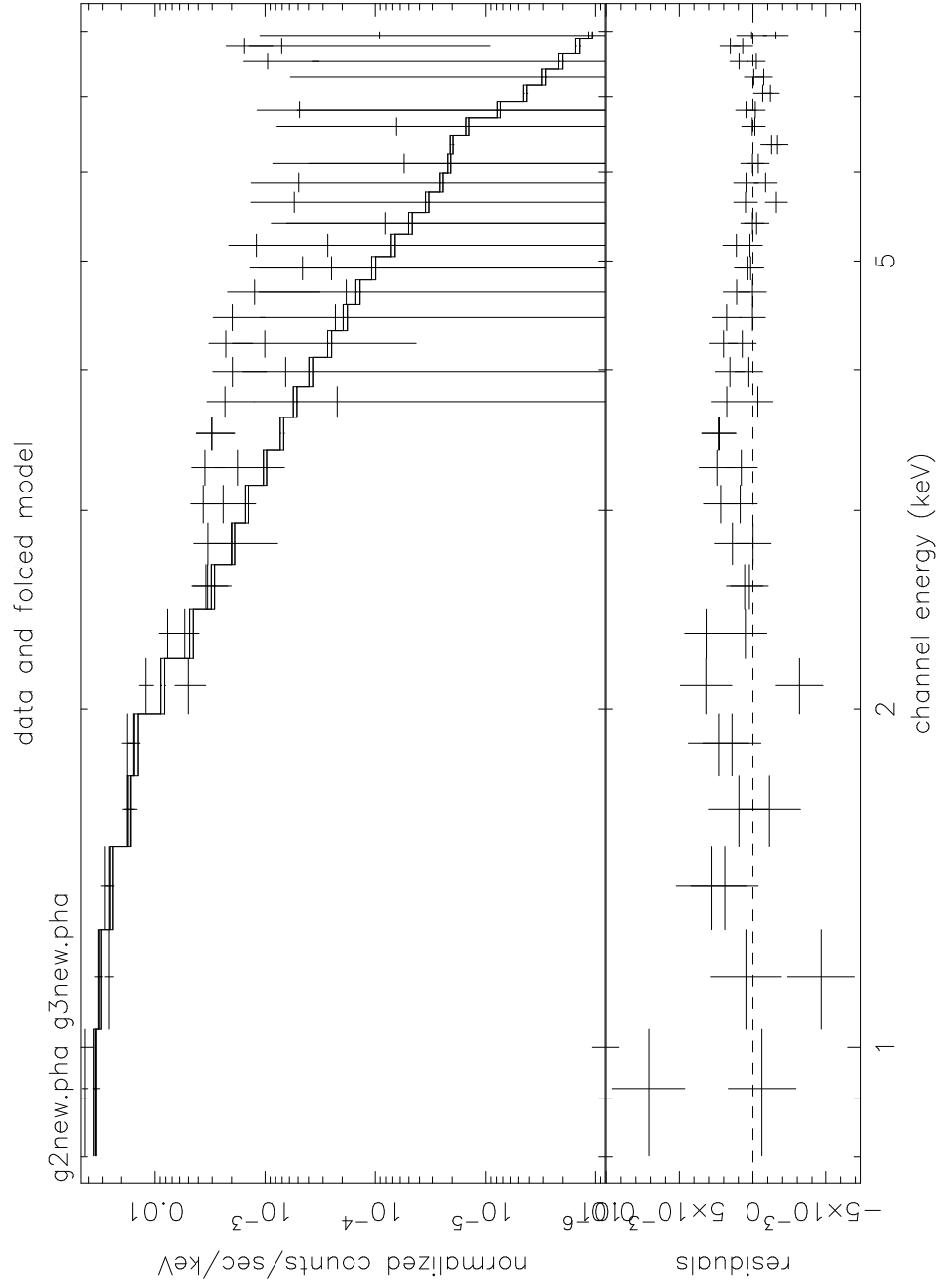


Fig. 10.— Same as Figure 9 but for A2197E.

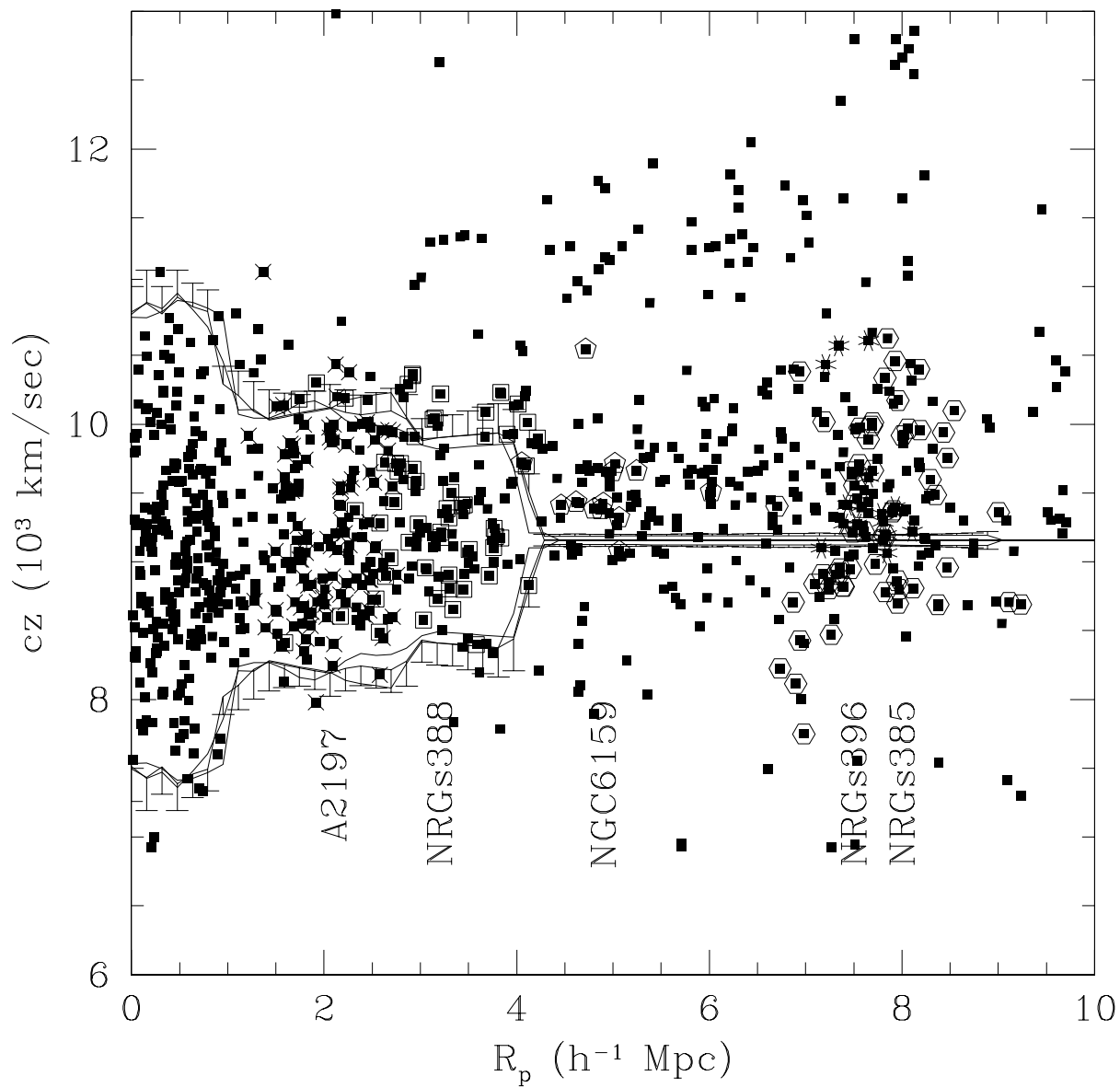


Fig. 11.— Projected radius versus redshift for galaxies surrounding A2199. Lines indicate our estimate of the caustics. Crosses, hexagons, open squares, asterisks, and pentagons indicate galaxies in A2197, NRGs385, NRGs388, NRGs396, and NGC6159 respectively.

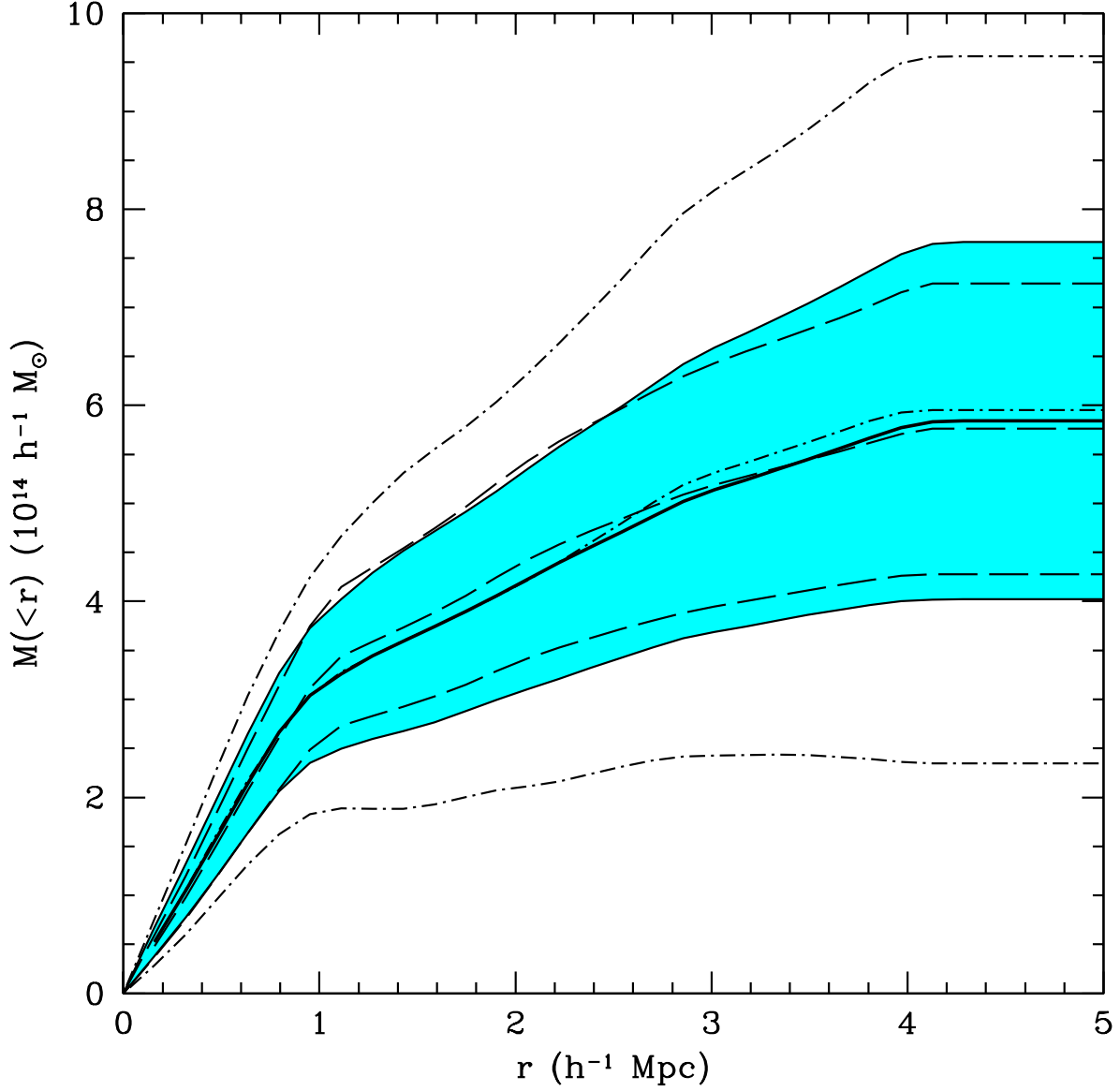


Fig. 12.— Mass profile of the A2199 supercluster. The thick solid line indicates the mass profile estimated using $q = 25$ (see text for definition), the thin solid lines and shaded region show the $1\text{-}\sigma$ uncertainties in this profile. The sets of dashed and dash-dotted lines indicate the mass profiles and $1\text{-}\sigma$ uncertainties for $q=10$ and 50 respectively.

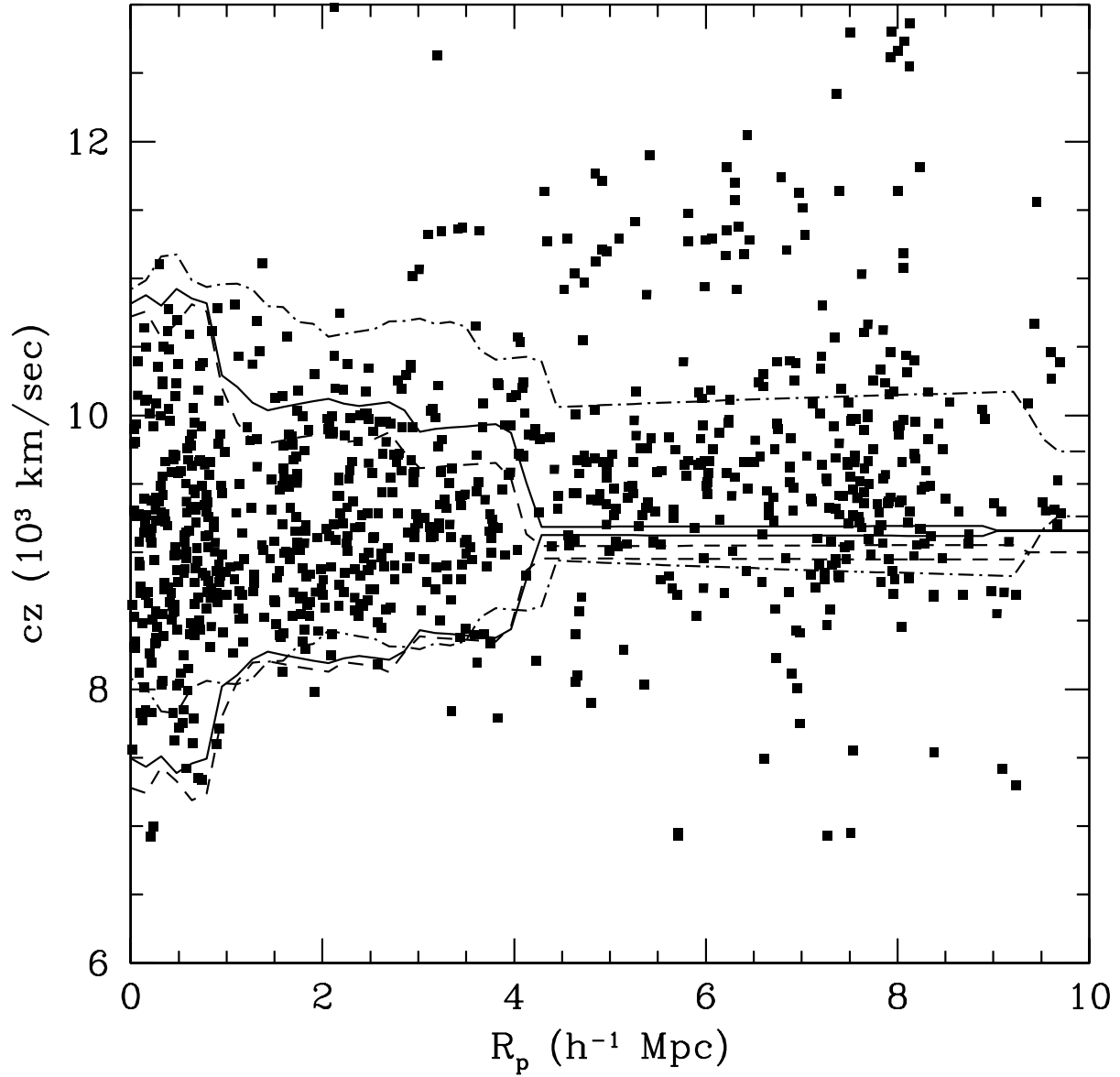


Fig. 13.— Same as Figure 11, but varying the systemic redshift of the supercluster cz_{sup} . Lines indicate our estimate of the caustics. Dashed, solid, and dash-dotted lines show the caustics calculated with $cz_{sup} = 9000, 9156,$ and 9500 km s^{-1} respectively.

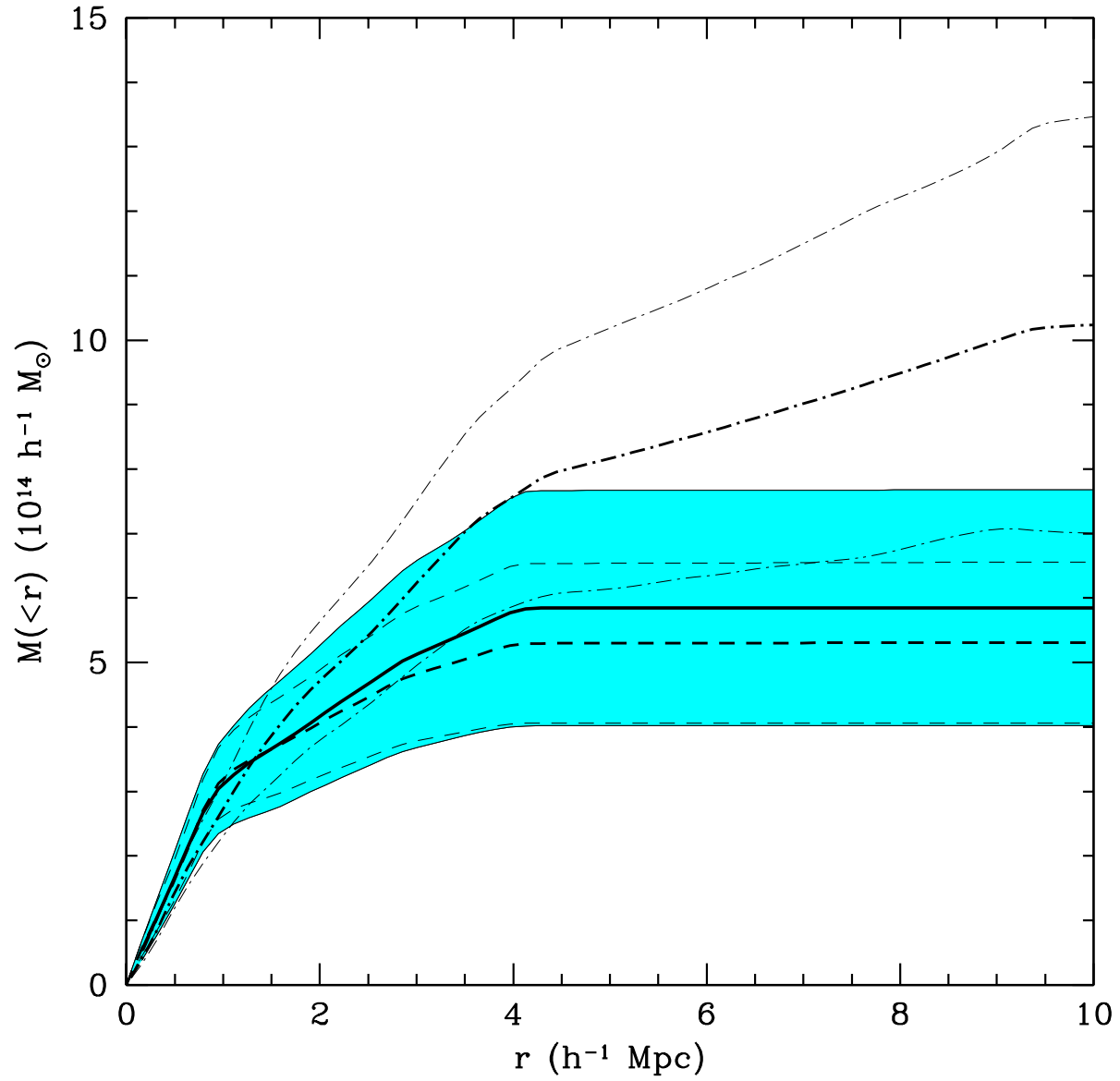


Fig. 14.— Effect on the mass profile of varying the central redshift of the supercluster. Dashed, solid, and dash-dotted lines show the caustics calculated with $cZ_{sup} = 9000$, 9156, and 9500 km s^{-1} respectively.

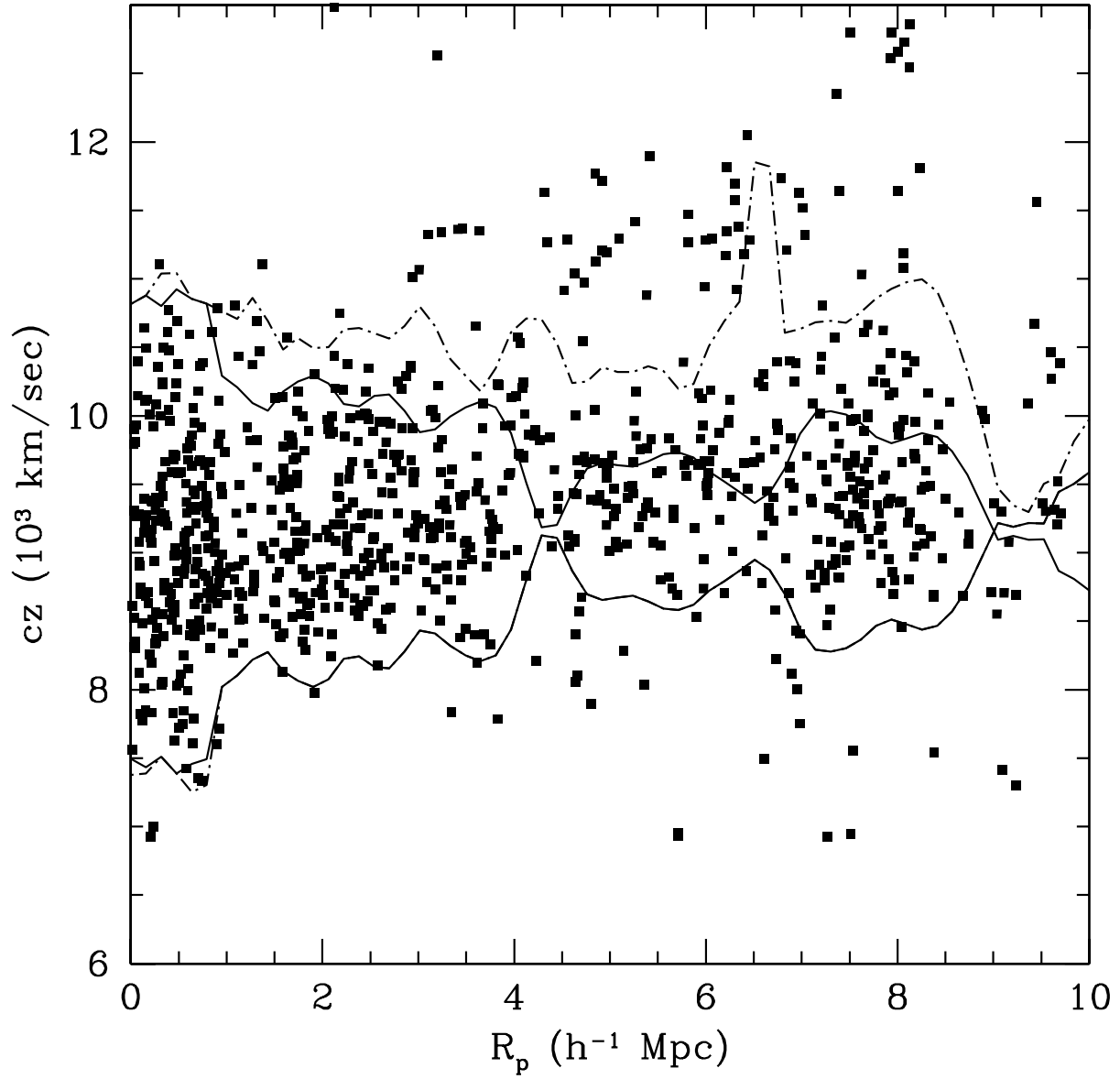


Fig. 15.— Same as Figure 11, but using relaxed requirements to calculate the caustics. Dashed lines show the caustics on either side of the cluster; the solid lines show the minimum caustic amplitude at each radius. The latter caustics are defined primarily by the lower caustic.

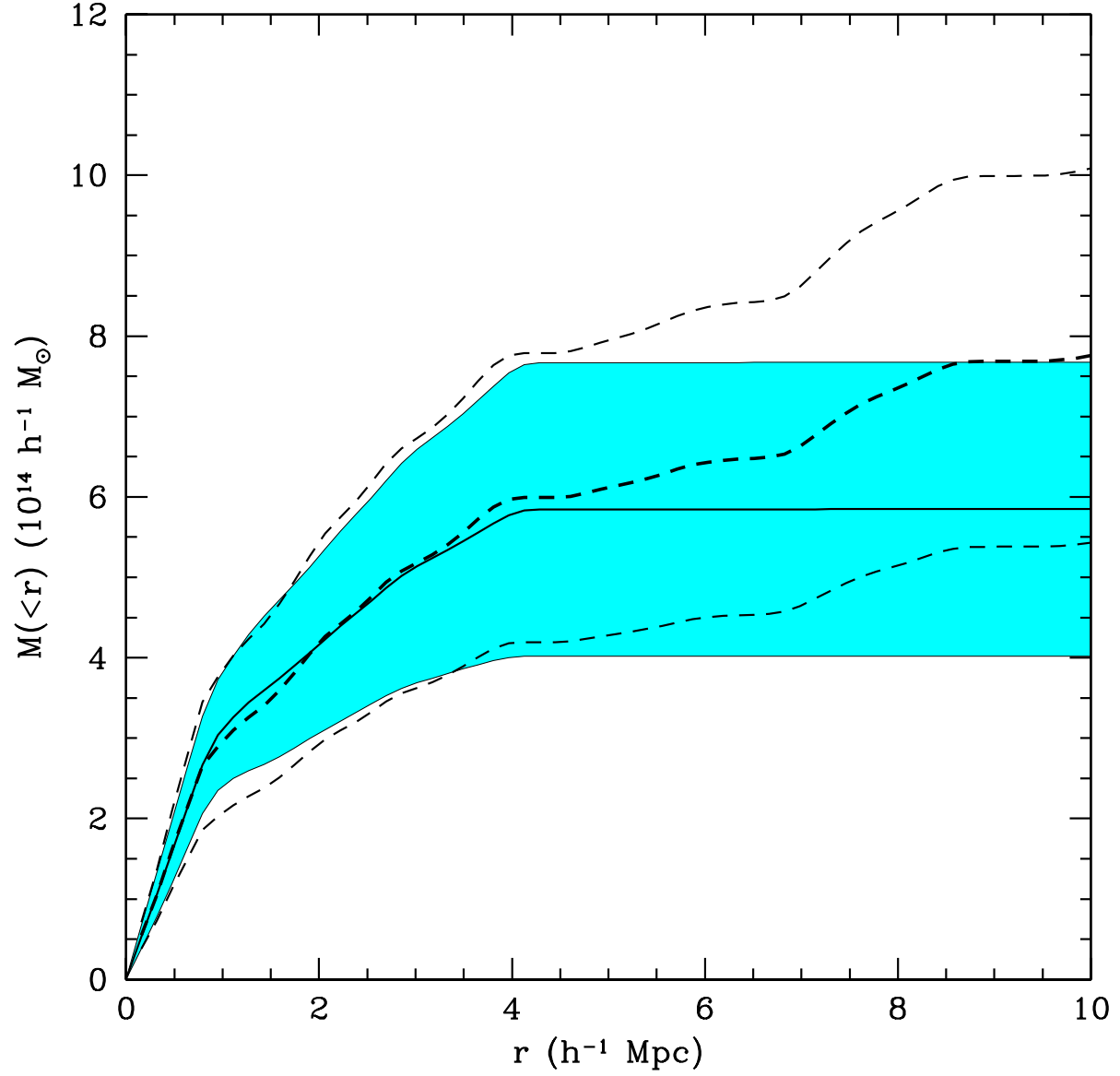


Fig. 16.— Mass profile calculated with relaxed requirements on the slope of the caustics. The dashed lines show the standard caustics for reference.

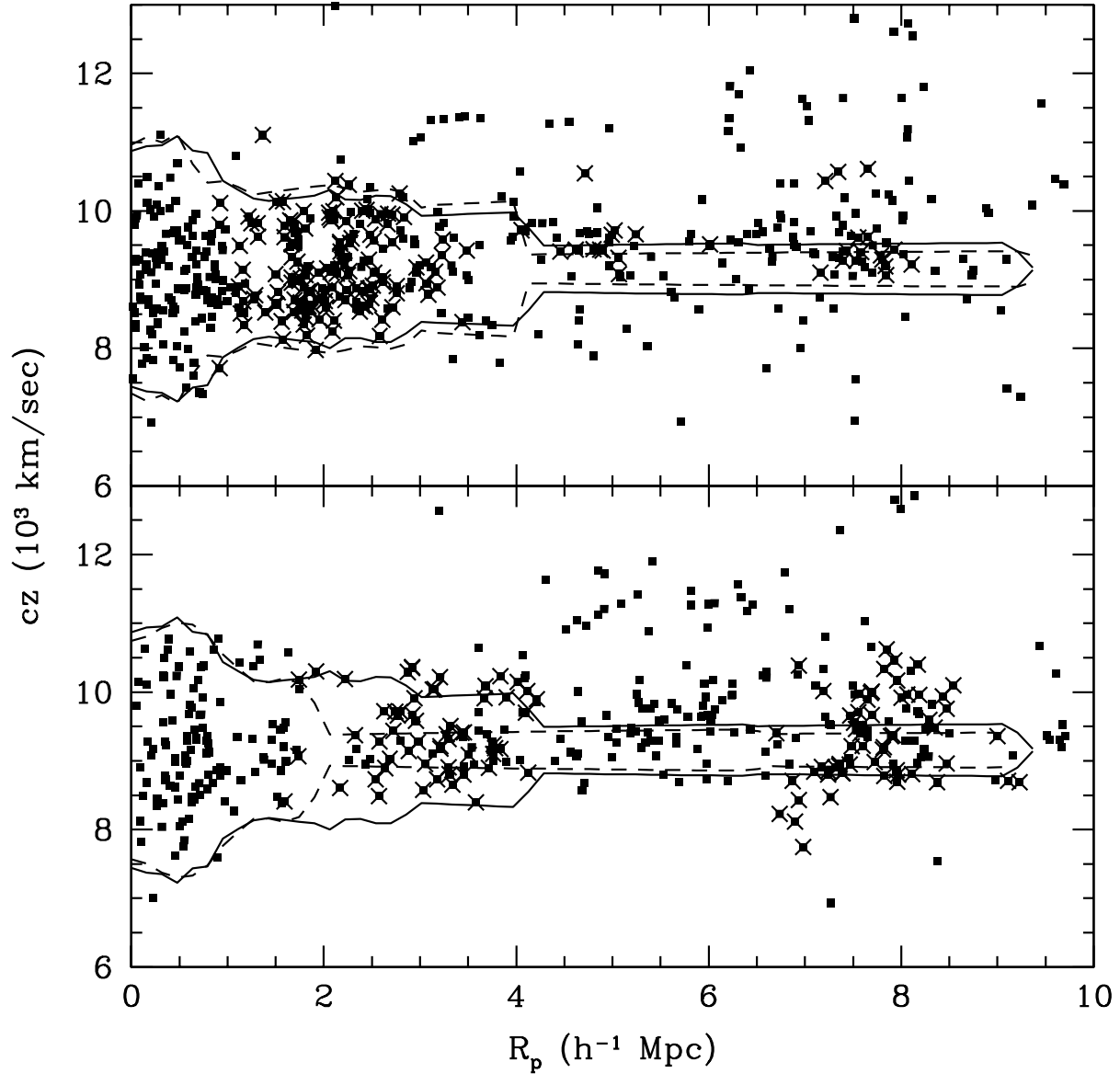


Fig. 17.— Projected radius versus redshift for galaxies surrounding A2199. The top panel shows galaxies towards A2197; the bottom panel shows galaxies away from A2197. Dashed lines indicate the caustics calculated for each sample; the solid lines are the caustics from the full sample. Crosses indicate galaxies in A2197, NGC 6159, and NRGs396 (top panel) and NRGs385 and NRGs388 (bottom panel).

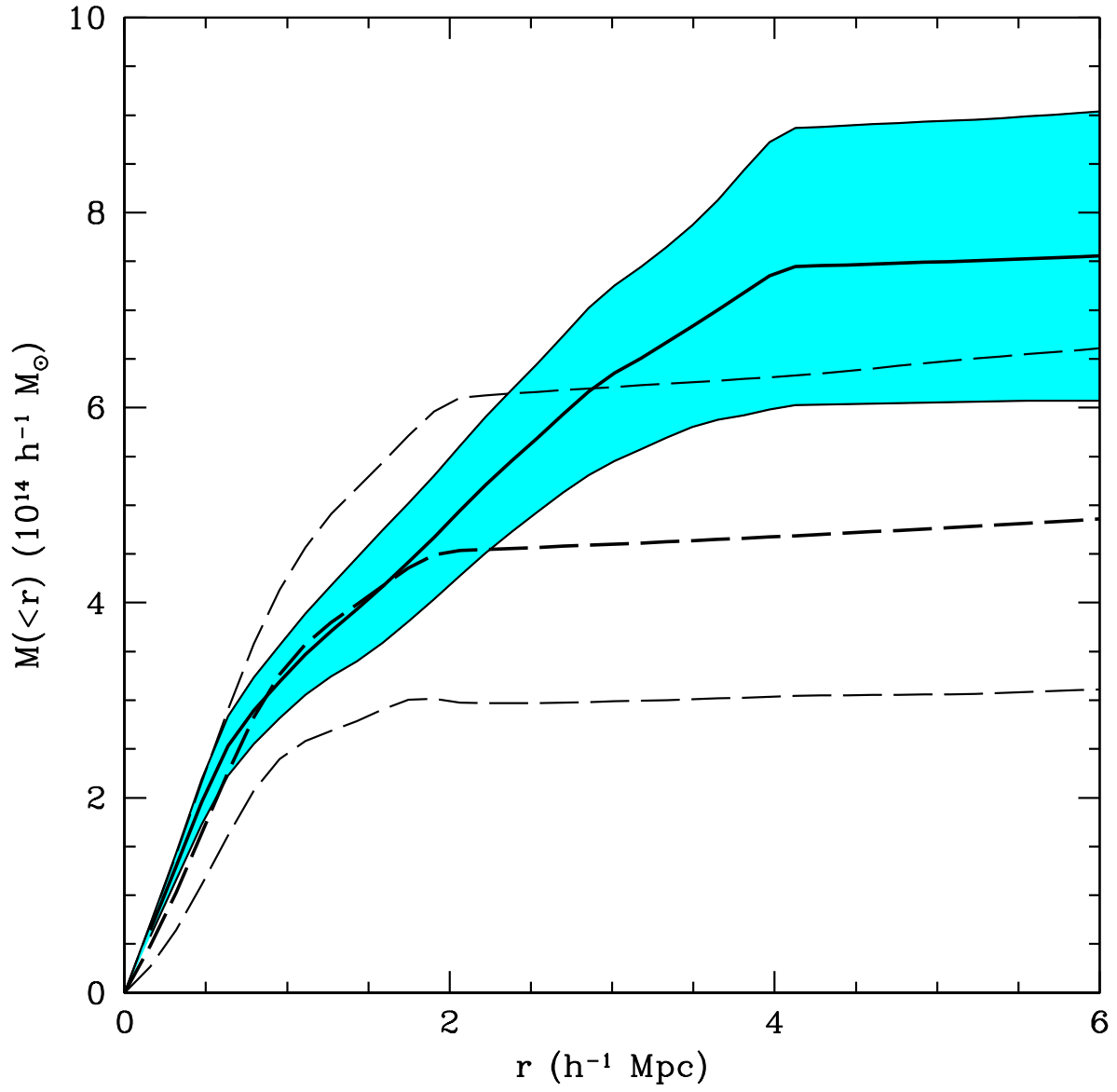


Fig. 18.— Mass profile calculated towards (solid lines) and away (dashed lines) from A2197.

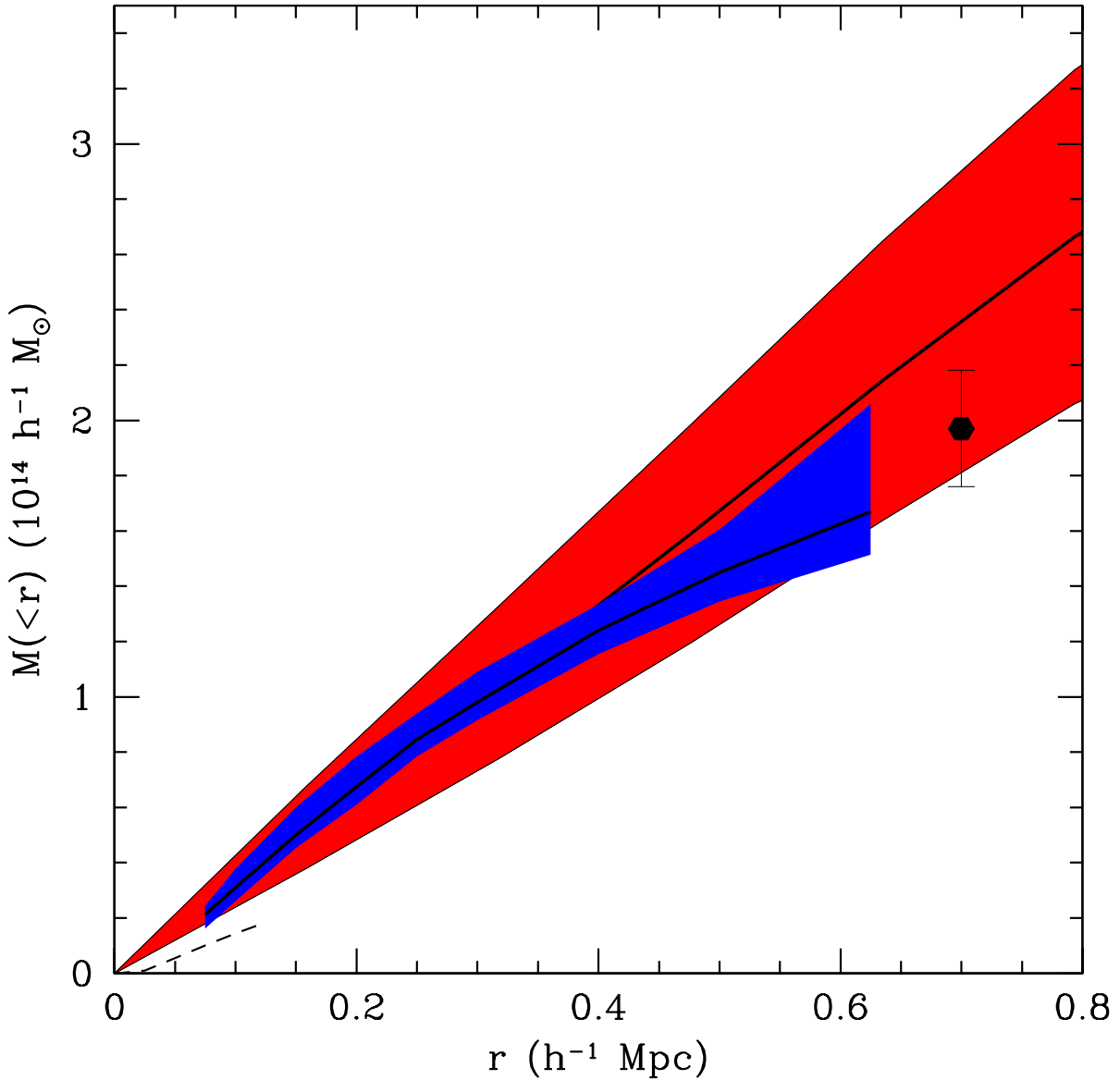


Fig. 19.— Comparison of infall mass profile to independent X-ray estimates. The $1\text{-}\sigma$ range of the infall mass profile is shown in red and the 90% confidence range of the X-ray mass profile is shown in blue. The NFW profile which best fits the X-ray data is indicated by a thick solid line. The point indicates a deprojected X-ray mass estimate and the dashed line shows the NFW profile which best fits *Chandra* X-ray data.

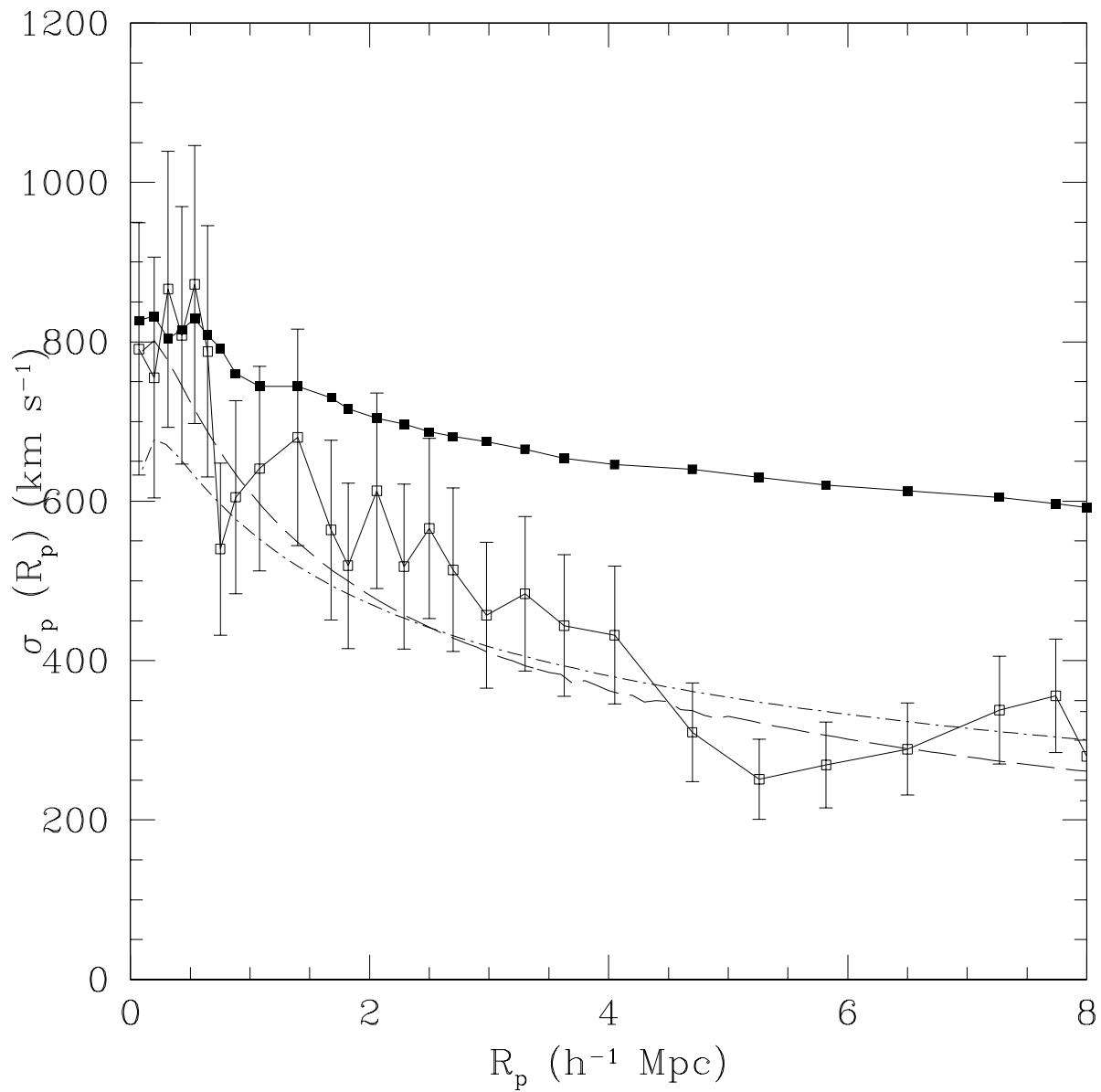


Fig. 20.— Velocity dispersion profile of A2199 member galaxies (open squares). Filled squares show the integrated velocity dispersion profile. Dotted and dot-dashed lines show the profiles predicted by the Hernquist and NFW profiles respectively assuming isotropic orbits. The predicted profiles have no free parameters.

Table 1: PROPERTIES OF SIMULATED SIMPLE SUPERCLUSTERS

System	M_1 $10^{13}h^{-1}M_\odot$	M_1/M_2	$M_{subhalo}$ $10^{13}h^{-1}M_\odot$	$R_{subhalo}$ $h^{-1}\text{Mpc}$
121	18.2	1.95	9.3	3.19
			8.8	3.55
			4.1	4.96
			4.7	5.87
156	33.5	4.43	7.6	2.90
			2.1	3.66
			1.2	6.74
			2.5	10.13
162	31.0	6.20	3.2	2.74
			5.0	3.38
			1.1	7.97
			2.0	8.89

Table 2: SIMULATED MASS PROFILE FIT PARAMETERS

System	Profile	a $h^{-1}\text{Mpc}$	$M(a)$ $10^{14}M_\odot$	χ^2	ν
121	NFW	0.24 ± 0.01	0.38 ± 0.02	101	23
121	Hernquist	0.49 ± 0.02	0.98 ± 0.05	167	23
121	SIS	0.5	0.42 ± 0.01	1152	24
156	NFW	0.18 ± 0.01	0.48 ± 0.02	18	23
156	Hernquist	0.41 ± 0.02	1.44 ± 0.07	64	23
156	SIS	0.5	0.93 ± 0.03	790	24
162	NFW	0.25 ± 0.01	0.71 ± 0.04	52	23
162	Hernquist	0.53 ± 0.02	1.93 ± 0.10	78	23
162	SIS	0.5	0.69 ± 0.02	1128	24

Table 3. Spectroscopic Data for A2199^a

RA (J2000)	DEC (J2000)	cz (km s ⁻¹)	σ_{cz} (km s ⁻¹)	Reference
15 57 54.36	+41 56 13.8	10387	125	04
15 57 58.01	+41 47 32.6	10464	033	04
15 57 59.40	+40 02 02.0	09300	000	04
15 58 47.35	+41 56 17.2	11561	033	04
15 59 28.85	+39 49 39.5	09296	045	04

^aThe complete version of this table is in the electronic edition of the Journal. The printed edition contains only a sample.

References. — (1) FAST spectra (2) Mohr et al. 2002, in prep.; (3) Mahdavi et al. 1999; (4) Falco et al. 1999; (5) Kirshner et al. 1983; (6) Strauss & Huchra 1988; (7) de Vaucouleurs et al. 1991; (8) Freudling et al. 1992; (9) Zabludoff et al. 1993; (10) Haynes et al. 1997; (11) Hill & Oegerle 1998.

Table 4: ARCHIVAL POINTED X-RAY OBSERVATIONS

System	Satellite	Instrument	Sequence	Live Time(ks)
A2199	ASCA	GIS/SIS	80023000	67
	ROSAT	PSPC	rp800644n00	41
A2197W	ROSAT	PSPC	rp800363n00/a01	13.5
	ASCA	GIS/SIS	85068000	45
A2197E	ROSAT	PSPC	rp800363n00/a01	13.5
	ASCA	GIS/SIS	85069000	49
NRGs385	ROSAT	PSPC	rp700508n00/a01	5.6

Table 5: PROPERTIES OF SYSTEMS ASSOCIATED WITH A2199

System	X-ray Coordinates		cz km s ⁻¹	σ_p km s ⁻¹	R_p h^{-1} Mpc	$\log L_X$ h^{-2} ergs s ⁻¹	$N_{3\sigma_p}$	N_{tot}
	RA (J2000)	DEC (J2000)						
A2199	16 28 38	39 33 05	9101±50	796 ⁺³⁸ ₋₃₃	–	44.1	255	339
A2197W	16 27 41	40 55 40	9144±52	584 ⁺⁴⁰ ₋₃₃	2.2	42.5	128	144
A2197E	16 29 43	40 49 12	9100±53	595 ⁺⁴² ₋₃₄	2.0	42.4	126	151
NRGs385	16 17 15	34 55 00	9308±86	643 ⁺⁶⁹ ₋₅₂	8.1	42.8	59	66
NRGs388	16 23 01	37 55 21	9421±74	563 ⁺⁶¹ ₋₄₆	3.1	42.3	58	78
NRGs396	16 36 50	44 13 00	9554±128	513 ⁺¹²⁸ ₋₇₃	7.7	42.0 ^a	16	29
NGC 6159	16 27 25	42 40 27	9566±95	344 ⁺¹⁰⁰ ₋₅₃	4.9	42.3 ^b	13	22

^aDetection significance = 2.7σ

^bHRI observation (Trinchieri & Pietsch 2000)

Table 6: PROPERTIES OF X-RAY SOURCES IN A2197 FIELD WITH OPTICAL COUNTER-PARTS

ID	Type	X-ray Coordinates (J2000)		cz km s ⁻¹	$f_X(0.1-2.4 \text{ keV})$ 10 ⁻¹² ergs cm ⁻² s ⁻¹	$\log L_X$ h ⁻² ergs s ⁻¹
		RA	DEC			
A2197W	Group	16 27 41	40 55 40	9408±77 ^a	3.13±0.10	42.5
A2197E	Group	16 29 43	40 49 12	8842±45 ^a	2.57±0.09	42.4
NGC 6146	Galaxy	16 25 10	40 53 34	8879±25	0.18±0.03	41.3
NGC 6150 ^b	Galaxy	16 25 50	40 29 19	8707±31	0.04±0.01	40.6
NGC 6175	Galaxy	16 29 58	40 37 43	8986±34	0.60±0.04	41.8
III Zw 078 ^b	Galaxy	16 26 46	40 41 40	8838±40	0.07±0.01	40.9
Anonymous ^c	Galaxy	16 28 26	40 51 39	9976±24	0.10±0.01	41.0
2MASXi J1626069+412046	Galaxy	16 26 07	41 20 39	17592±21	0.05±0.01	41.3
A2187	Cluster	16 24 11	41 13 46	54938±54 ^a	2.37±0.08	44.2
A2196	Cluster	16 27 26	41 29 55	38811±30 ^a	1.28±0.06	43.6
FBQS J162901.3+400759	QSO	16 29 01	40 08 34	81545 ^d	1.41±0.06	44.3
KUV 16295+4054	QSO	16 31 13	40 48 40	77048 ^e	1.54±0.08	44.5

^aRedshift of bright galaxy near center

^btentative identification, X-ray-optical separation $\sim 1'$

^csee also Knezek & Bregman (1998)

^dBade et al. (1995)

^eCrampton et al. (1992)

Table 7: MASS PROFILE FIT PARAMETERS

Method	Profile	q	a $h^{-1}\text{Mpc}$	$1 - \sigma$ $h^{-1}\text{Mpc}$	$M(a)$ $10^{14}M_{\odot}$	$1 - \sigma$ $10^{14}M_{\odot}$	χ^2	ν
Standard	NFW	10	0.17	0.13-0.21	0.51	0.45-0.58	1.2	24
Standard	Hernquist	10	0.50	0.43-0.59	1.75	1.60-1.90	1.1	24
Standard	SIS	10	0.5	–	1.01	0.97-1.06	36.1	25
Standard	NFW	25	0.14	0.11-0.19	0.47	0.40-0.55	0.5	25
Standard	Hernquist	25	0.47	0.39-0.57	1.68	1.50-1.85	1.2	25
Standard	SIS	25	0.5	–	1.00	0.94-1.05	28.8	26
Standard	NFW	50	0.15	0.10-0.23	0.49	0.36-0.65	0.2	23
Standard	Hernquist	50	0.46	0.33-0.64	1.65	1.35-2.05	0.4	23
Standard	SIS	50	0.5	–	1.08	0.96-1.18	7.5	24
$cz_{sup} = 9000$	NFW	25	0.13	0.10-0.15	0.43	0.37-0.48	1.7	23
$cz_{sup} = 9000$	Hernquist	25	0.42	0.36-0.49	1.53	1.40-1.66	1.5	23
$cz_{sup} = 9000$	SIS	25	0.5	–	0.97	0.93-1.02	52.0	24
$cz_{sup} = 9500$	NFW	25	0.30	0.26-0.34	0.79	0.73-0.86	2.1	61
$cz_{sup} = 9500$	Hernquist	25	0.94	0.86-1.04	2.80	2.62-2.96	10.2	61
$cz_{sup} = 9500$	SIS	25	0.5	–	0.81	0.78-0.85	121	62
Relaxed	NFW	25	0.15	0.11-0.19	0.46	0.41-0.52	0.6	54
Relaxed	Hernquist	25	0.63	0.52-0.75	1.96	1.82-2.11	2.5	54
Relaxed	SIS	25	0.5	–	0.59	0.56-0.62	69.0	55

Table 8: PREDICTED AND OBSERVED VELOCITY DISPERSIONS

System	L_X	T_X	σ_{p,L_X}	σ_{p,T_X}	σ_p
A2199	44.1	4.5	892	810	796^{+38}_{-33}
A2197W	42.5	1.55	357	423	584^{+40}_{-33}
A2197E	42.4	0.96	337	316	595^{+42}_{-34}
NRGs385	42.8	–	424	–	643^{+69}_{-52}
NRGs388	42.3	–	318	–	563^{+61}_{-46}
NRGs396	42.0	–	268	–	513^{+128}_{-73}
NGC6159	42.3	–	318	–	344^{+100}_{-53}